UNIVERSITY OF OKLAHOMA

GRADUATE COLLEGE

MODELING OF NON-EQUILIBRIUM EFFECTS IN PARTICULATE FLOW THROUGH POROUS MEDIA

A THESIS

SUBMITTED TO THE GRADUATE FACULTY

in partial fulfillment of the requirements for the

Degree of

MASTER OF SCIENCE

By

YI JIN
Norman, Oklahoma
2018

MODELING OF NON-EQUILIBRIUM EFFECTS IN PARTICULATE FLOW THROUGH POROUS MEDIA

A THESIS APPROVED FOR THE
MEWBOURNE SCHOOL OF PETROLEUM AND GEOLOGICAL ENGINEERING

BY

Dr. Rouzbeh G. Moghanloo, Chair

Dr. Siddharth Misra

Dr. Bor-Jier (Ben) Shiau

Dedicate to my dear mom and dad who gave me countless love and support

Acknowledgements

First and foremost, I would like to express my sincere gratitude to my advisor, Dr. Rouzbeh Ghanbarnezhad Moghanloo, for his guidance, assistance, and support during my graduate studies. It is his generous help and invaluable advice that enable me to accomplish this thesis. The door to his office was always open whenever I ran into a trouble spot or had a question about my research or writing. I appreciate his support on providing COMSOL license, which has made a great contribution to this work.

I would also like to acknowledge Dr. Siddharth Misra and Dr. Bor-Jier (Ben) Shiau for serving as my committee members and reviewing my thesis. I learned lots of valuable knowledge that may help me in the future work through their courses and advices.

Furthermore, I would like to appreciate Dr. Davud Davudov and Dr. Da Zheng for their assistances on my research. Their intelligent knowledge always give me inspirations on my work. I would also like to thank my fellow and friend Xu Yan who gave me great helps during my graduate studies. Moreover, I would like to say thank you to my friends Hao Zhang, Zhaoyi Zhuo, Yue Fang, and Xiameng Peng for their accompanies during my undergraduate life at OU.

Finally, I would like to express my deepest appreciation to my parents whose love are with me in whatever I pursue. Their unfailing support and continuous encouragement throughout my study years provide me solid foundation to accomplish this thesis. They are always my life-coaches.

Table of Contents

List of Tables

List of Figures

Abstract

The complex dynamics of fluid and particles flowing through pore space demands some relaxation time for particles to catch up with fluid velocity which manifest themselves as non-equilibrium (NE) effect. Previous studies have shown that NE effect in particulate transport can have significant consequences when relaxation time is comparable to the characteristic time associated with the fluid flow field. However, the existing models are lacking to account for this complicated relation between particles and fluid.

In this thesis study, the general form of harmonic oscillation equation is adapted to describe NE effects in particulate flow system. The NE effect is evaluated by solving coupled mass balance equations with computational fluid dynamic (CFD) techniques within COMSOL Multiphysics®. Simplified straight tube model, periodic converging-diverging tube model and SEM image of a real pore network are applied in the NE analyses.

The results indicate that two key parameters of oscillator equation, amplitude (A) and damping ratio (ζ) can be used to explain the NE effect between particle and fluid. The former parameter represents the magnitude of NE and the latter is an indication of flow path geometry as well as time needed to attain equilibrium. The sensitivity analyses imply that fluid viscosity, flow channel size, and flow pattern affect the magnitude of the NE effect. By conducting simulation on the SEM image of a real pore structure, the equivalent radii of the pores that particles move through were obtained.

Chapter 1: Introduction

1.1 Scope of the Problem

Particle transport behavior is the issue that petroleum engineers attempted to solve for many years because particulate flow systems exist in a wide range of petroleum related processes, for example the injection of seawater during water flooding, invasion of filtrate during drilling, and micro enhanced oil recovery (Yuan et al. 2016). The formation damage caused by fine particle retention and detachment highly effect the productivity and injectivity of wells (Bedrikovetsky et al. 2011). A large amount of fines production may also result in equipment erosion, flowlines plugging, and other potential hazards (Marquez et al. 2014). In the asphaltene deposition problem, asphaltene particles can change to accumulate or adsorb onto the pore surfaces, which leads to pore plugging in the reservoir and finally affects the flow rate within the wellbore (Davudov et al. 2018). During proppant placement process, the performance of proppant packs in hydraulic fracture plays a significant role in fracture conductivity and production behavior (Fan et al. 2018). It is believed that uniform distribution of proppant provides highest fracture conductivity. However, it is very challenging to sustain uniform distribution because of proppant settlement and embedment (Yu and Sepehrnoori. 2013). Therefore, it is extremely important for petroleum engineers to understand particle transport behavior in order to apply it in those aforementioned petroleum processes. Engineers have derived many mathematical models and conducted several experiments to investigate the particle transport mechanisms in particulate systems. In the previous researches of particle transport in particulate flow through porous media, it has been

observed that the particle velocity does not necessarily have the same velocity as its carrier fluid when moving through pore networks. This complex dynamic between particle and fluid in porous media has drawn people's attention to investigate the mechanism behind it and how it influences particle transport behavior.

1.2 Thesis Objectives

The objectives of this thesis are as follows:

1. Applying finite element software to model the NE effect between particles and the carrier fluid.
2. Evaluating the NE effects in particulate flow system quantitatively using adapted harmonic oscillation equation. Then use the non-equilibrium equation to decouple particle transport equation from fluid flow equation.
3. Investigating how fluid property and flow channel geometry affect the NE effects
4. Using NE study to obtain the equivalent tube radii for a pore structure through which particles move.

1.3 Thesis Outline

The thesis is driven by the following hypothesis: *the linear theory of stability can explain non-equilibrium evolution in particulate systems through general form of harmonic oscillation equation*. Chapter 2 presents a background and literature review of the mechanism of particle-fluid interaction in the porous media. Moreover, practical particle transport problems including fines migration and enhance oil recovery (EOR) using nanoparticle flooding are covered. Meanwhile, the non-equilibrium effects in fluid-fluid system is reviewed to give idea to model particle-fluid non-equilibrium effects.

Finally, how petroleum engineers use computational fluid dynamics (CFD) techniques to model particle transport process is presented.

Chapter 3 provides the methodology of using CFD technique to model particle transport in fluid flow and adapting harmonic oscillation equation to describe the NE effect between particle and carrier fluid.

Chapter 4 covers the modeling of particle transport behavior in simplified flow geometries, including straight tube and periodic converging-diverging tube. The NE effects between particle and fluid were investigated. Moreover, the sensitivity analyses on fluid property in different flow path geometries are included in this chapter.

Chapter 5 covers the continuous study of non-equilibrium effect in particulate flow through actual pore structure. The determination of equivalent tube radii for the complex pore structure that particles move through is addressed.

Chapter 6 highlights the conclusions and outcomes of this thesis study as well as the future recommendations.

Chapter 2: Literature Review

2.1 Fluid-Fluid Interaction and Non-equilibrium Phenomena

Bottero et al (2011) conducted series of experiment of injecting PCE (etrachloroethylene) to fully water-saturated column using high pressure to investigate non-equilibrium capillarity effects in two phase flow. The non-equilibrium effects equation of capillary pressure was derived by Hassanizadeh and Gray (1990) and Kalaydjian (1992), and it can be seen in **Eq. 2.1**.

$$P_n - P_w = P_c\left(S_w\right) - \tau\left(S_w\right)\frac{\partial S_w}{\partial t} \tag{2.1}$$

It relates the difference of two fluids pressure ($P_n - P_w$) with capillary pressure (P_c) and changing of water saturation with time. τ is a dynamic capillarity coefficient. The experiment results in shown in **Fig 2.1**. They observed that the non-equilibrium occurred mainly at the early stage of the experiment. In addition, the non-equilibrium pressure difference between wetting and non-wetting phase can only observed at high pressure injection experiment. In **Fig 2.1 (c)** and **(f)**, the pressure differences increase significantly to overshoot values and then get decrease and finally stabilized in a certain value. This behavior is caused by non-equilibrium effect at the interface of wetting and non-wetting phase.

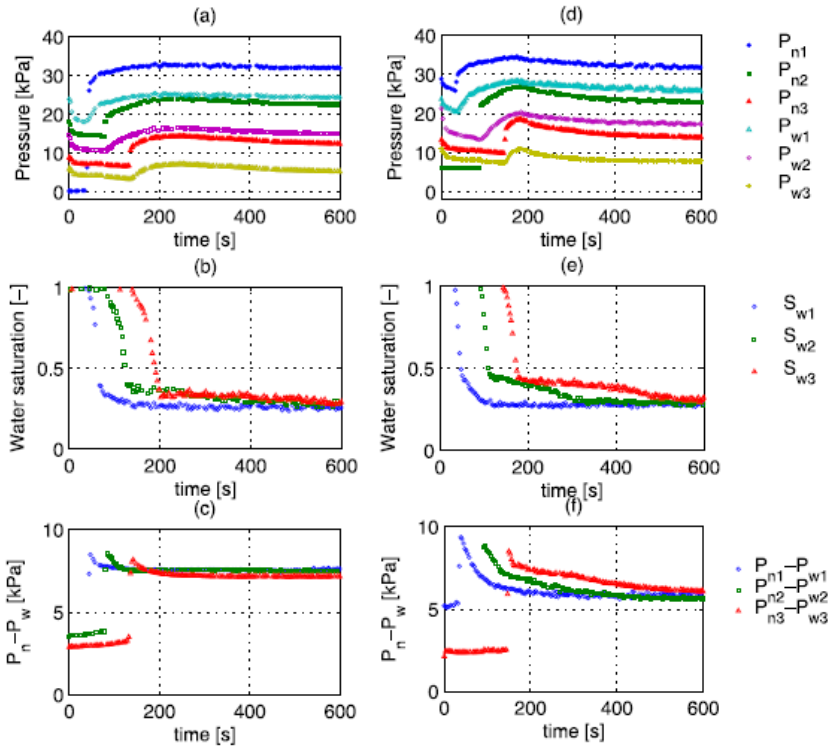

Figure 2.1: Results of non-equilibrium experiments. (c) and (f) present the differential pressures of wetting and non-wetting phases during the experiment (Bottero et al. 2011).

Yassin et al (2017) has studied and observed the non-equilibrium effect during CO_2/oil interaction. They conducted an experiment of injecting CO_2 in gas, liquid, and superficial states to oil to visualize the interaction of two phase under non-equilibrium condition. They found that there were pressure declines from the buildup pressure under socking processes at the interface of CO_2 and oil. One of the soaking process is demonstrated in **Fig 2.2**. It was observed that the extracting flow, which flowed upward and the condensing flow, which flowed downward appeared at the interface of CO_2 liquid and oil phase. The liquid CO_2 dissolved into oil phase during socking process. Moreover,

there were solid precipitates attached on the glass near the interface. It was because of the asphaltenes deposition under a specific molar fraction of CO_2 and a certain pressure.

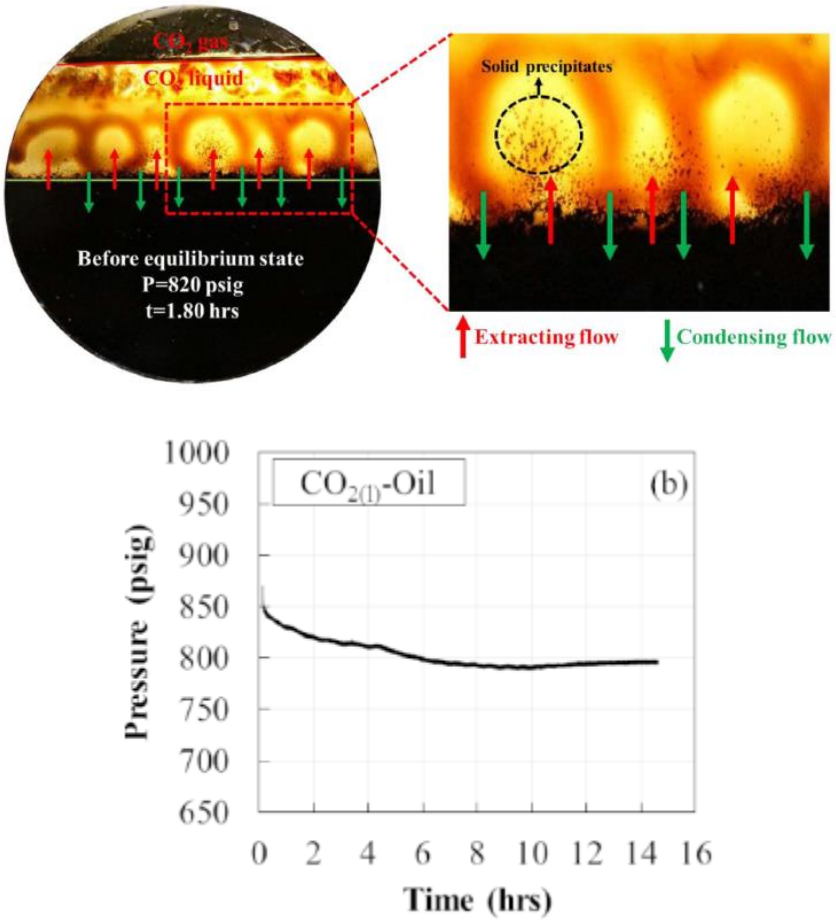

Figure 2.2: The visualized non-equilibrium phenomena occurred at the interface of liquid CO_2 and oil (top) and the pressure drop during the experiment (bottom) (Yassin et al. 2017).

2.2 Particle-Fluid Interaction

2.2.1 Liner Momentum Coupling

Linear momentum coupling between phases happens because of mass transfer and interface drag and lift (Crowe. Et al. 2012). The general form of liner momentum coupling between particle and fluid can be expressed as **Eq. 2.2**.

$$m\frac{dv_i}{dt} = mg_i + V_d\left(-\frac{\partial p}{\partial x_i} + \frac{\partial \tau_{ij}}{\partial x_j}\right) + 3\pi\mu_c D\left[\left(u_i - v_i\right) + \frac{D^2}{24}\nabla^2 u_i\right] + \frac{1}{2}\rho_c V_d\frac{d}{dt}\left[\left(u_i - v_i\right) + \frac{D^2}{40}\nabla^2 u_i\right] + \frac{3}{2}\pi\mu_c D^2\int_0^t\left[\frac{d/d\tau\left(u_i - v_i + D^2/24\times\nabla^2 u_i\right)}{\pi\nu_c\left(t-\tau\right)^{1/2}}\right]d\tau \tag{2.2}$$

where m is the mass of particle. The first term on the right side of the equation is called body force due to gravity. The second term represents the pressure and shear stress in undisturbed flow. The third terms is the steady state drag force. The last two terms are the virtual mass term and Basset term, respectively. They can only be used in unsteady state flow.

2.2.2 Steady-State Drag Forces

The steady state drag force is the drag force acting on the particle in the velocity field that generated by carrier fluid when there is no acceleration of the relative velocity between particle and fluid (Crowe. Et al. 2012). The basic equation can be expressed as

$$F_{ss,i} = 3\pi\mu_c D\left(u_i - v_i\right) + \mu_c\pi\frac{D^3}{8}\nabla^2 u_i \tag{2.3}$$

The second term of the equation is called Faxen force, which is used to correlate to Stokes drag for the curvature of velocity field. As for a straight flow field, the Faxen force equal to zero.

For straight fluid flow, the drag force can be written in terms of drag coefficient as

$$F_{ss,i} = \frac{1}{2}\rho_c C_D A|u_i - v_i|(u_i - v_i) \tag{2.4}$$

where C_D is the drag coefficient, A is the area of the particle, u_i and v_i are the continuous phase (fluid) velocity and disperse phase (particle) velocity. The drag coefficient highly depends on the Reynolds number. **Fig 2.3** demonstrates the relationship between drag coefficients with Reynolds number.

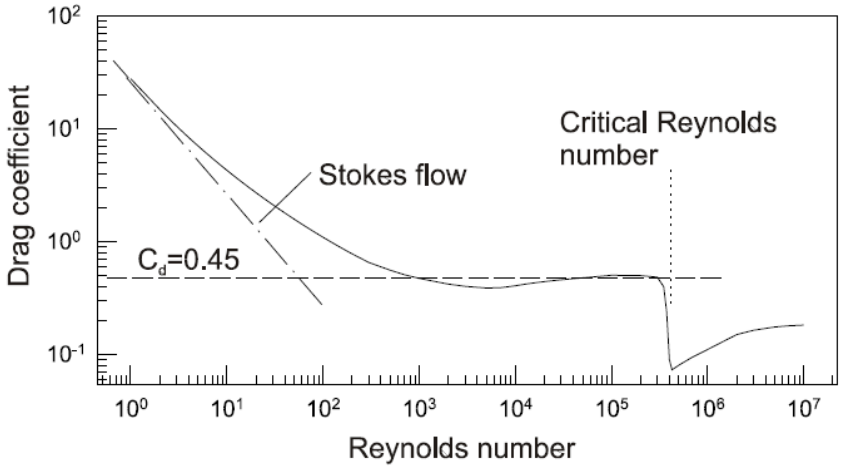

Figure 2.3: Change of the drag coefficient with Reynolds number (Crowe. Et al. 2012)

The flow at low Reynolds number (Re < 1) where drag coefficient changes inversely with Re number is referred to as Stocks flow regime. In the Stocks flow, the inertial terms in the Navier-Stokes equations are not important; therefore, they can be neglected. The governing equation is

$$\frac{\partial p}{\partial x_i} = \mu_c \frac{\partial^2 u_i}{\partial x_i \partial x_j} \tag{2.5}$$

Drag force is generated because there is pressure difference on two sides of spherical particle. The force that moves the fluid adjacent to the surface has to against the shear force. The two forces can be written as

$$F_p = \pi \mu_c DU \tag{2.6}$$

$$F_\tau = 2\pi \mu_c UD \tag{2.7}$$

The total drag force is the sum of the two contributions, and it can be expressed as

$$F_D = 3\pi \mu_c DU \tag{2.8}$$

Put the drag force equation back to **Eq. 2.4**, the drag coefficient can be obtained

$$C_D = \frac{24}{\mathrm{Re}_r} \tag{2.9}$$

where Re_r is the Reynolds number base on relative velocity.

2.2.3 Unsteady-State Drag Forces

When small fluid drop or particle flows in a viscous fluid at a small Reynolds number not only influenced by Stokes drag but also another drag force called memory-integral drag, also known as Boussinesq-Basset drag (the last term in **Eq. 2.2**), particles can experience an oscillatory motion under the effect of external forces (Hassan et al, 2017). In this case, the resonance curve including shape, amplitude, and quality of oscillator become important. Those characteristics of particle oscillator under the effect of Stokes drag has already been investigated.

2.3 Fines Migration Problem

2.3.1 Mechanism of Fine Detachment

The forces acting on single particle that attach to grain surface are drag force (F_d) from viscous fluid flow, electrostatic force (F_e), lifting force (F_l), and buoyancy force (F_g) (Yuan et al. 2015). The force balance of single particle is illustrated in **Fig 2.4**.

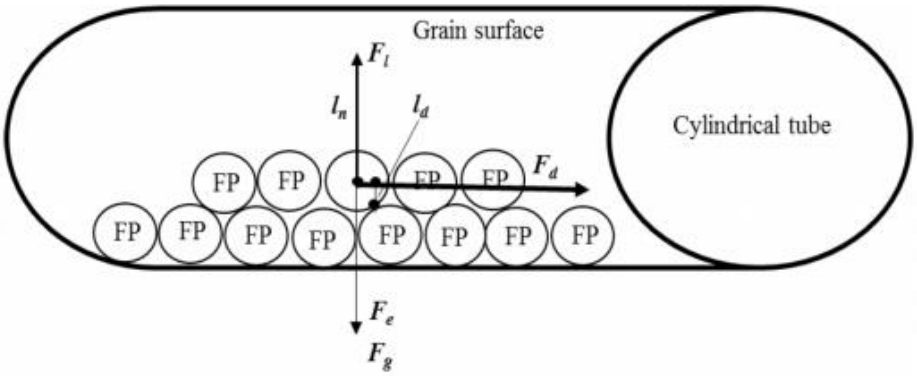

Figure 2.4: Schematic of forces exerting on single fine particle (Yuan et al. 2015)

Particle will be detached if the detaching torque of drag and lifting forces exceeds the attaching torque generated by electrostatic force and gravity force; otherwise the particle will attach on the grain surface (Oliveira et al. 2014).

2.3.2 Governing Equations for Fines Migration

The commonly used governing equation of fines migration involves particle suspension, retention and straining (Yu et al. 2018). The mass balance equation is described as

$$\frac{\partial\left(\phi s\left(\sigma\right)c+\sigma\right)}{\partial t}+U\frac{\partial cf\left(\sigma\right)}{\partial x}=0 \tag{2.10}$$

where, ϕ is porosity, s is accessibility factor, c is suspended fines concentration, σ is retained fines concentration, U is Darcy velocity, and f is drift-delay factor. The rate of fines straining is defined as

$$\frac{\partial \sigma}{\partial t} = \lambda(\sigma) f(\sigma) Uc \tag{2.11}$$

where, λ is the filtration coefficient.

Yuan and Shapiro (2010) had observed that the velocity of particle that near the pore surface is less than the velocity of its carrier fluid. To model the fine particle velocity, a drift-delay factor (alpha) is introduced to describe the slow particle motion near the pore surface (Oliveira et al. 2014). The drift-delay factor is defined as

$$\alpha = \frac{f}{s} = \frac{U_s}{U} \tag{2.12}$$

where U_s is the fines rolling velocity. The drife-delay factor can be used to decouple particle and fluid veloctiy when solving particle and fluid equation (Russel et al. 2018).

2.3.3 Experiment of Water Flooding with Fines Migration

Hu et al (2016) conducted a core flooding experiment to explain nanoparticle assists water flooding during EOR process. The experiment instrument is presented in **Fig 2.5**.

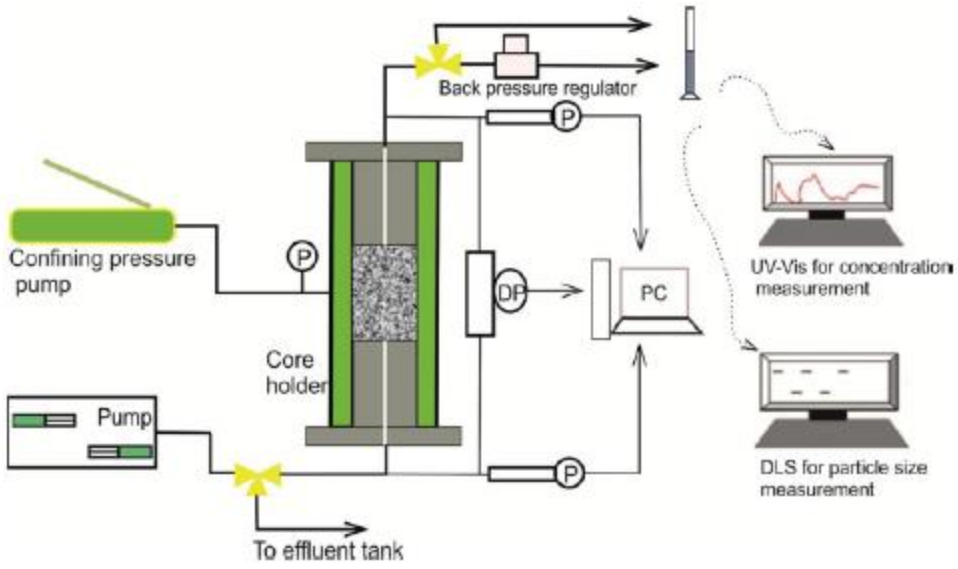

Figure 2.5: Schematic of experiment apparatus and flow diagram for water flooding (Hu et al. 2016)

The fluid was injected through the core sample vertically upward. The whole core flooding process contains three stages: 1). water-flooding with only the synthetic brine 2). water-flooding with the synthetic brine and the nanoparticle stabilizer, and 3). nano-flooding with different concentrations of nanoparticles. They investigated the nanoparticle migration behavior during flooding. The experimental results can be seen as **Fig 2.6**.

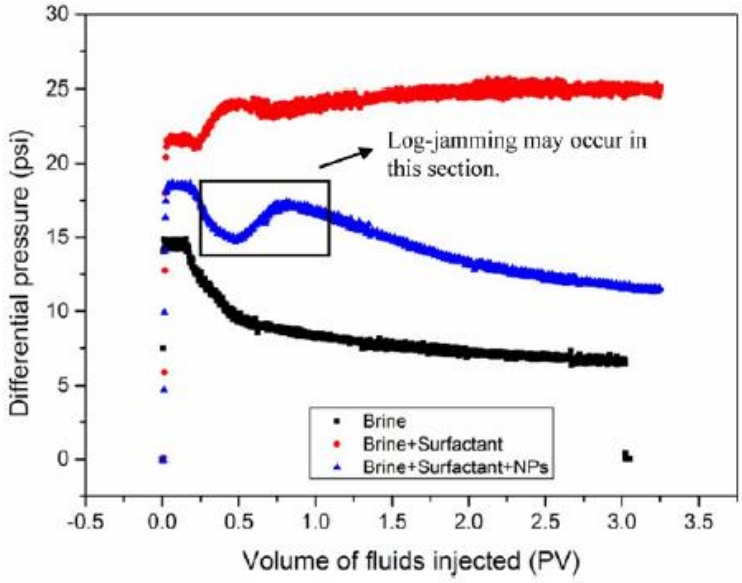

Figure 2.6: Differential pressure profile for brine, brine with surfactant, and nano-fluid flooding (Hu et al. 2016)

The results shown that nanoparticle flood had higher pressure drop compared with that of brine flooding. In nanoparticle flooding, there was a pressure increase, which is highlighted in the figure. It is because nanoparticles were temporarily stuck in the core, which is called log jamming.

Russel et al (2018) had same observation during their experiment on coreflood of artificial sand-kaolinite core. They measured the pressure drop during the injection period. The result is shown in **Fig 2.7**. It has been observed that there were pressure drop decreases during the coreflood experiment.

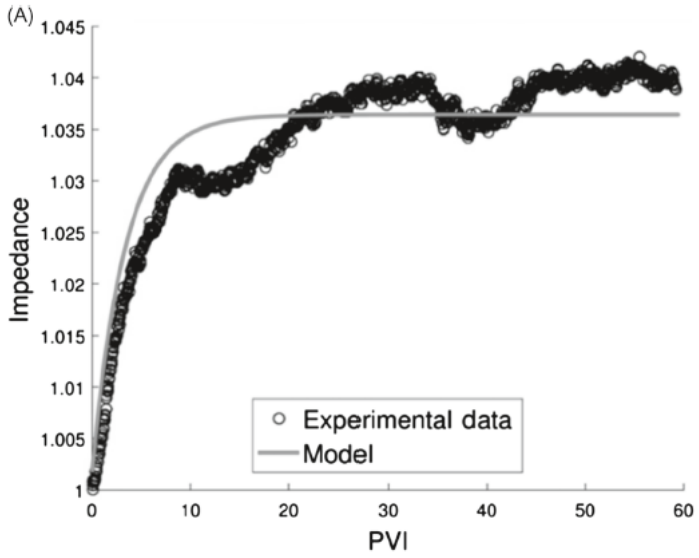

Figure 2.7: Coreflood experiment data with the model for velocity-induced fines migration. Core Impedance refer to as dimensionless pressure drop. PVI stands for the number of pore volume injected (Russel et al. 2018)

Log jamming is one of the mechanisms that cause pore plugging (Sun et al. 2017). The mechanism is demonstrated in **Fig 2.8**. When nanofluid flows from pores to throats, the flowing channel area become narrow causing the increase of nanofluid velocity. The fluid velocity will become faster than nanoparticles. It causes nanoparticles accumulate at the entrance of pore throat.

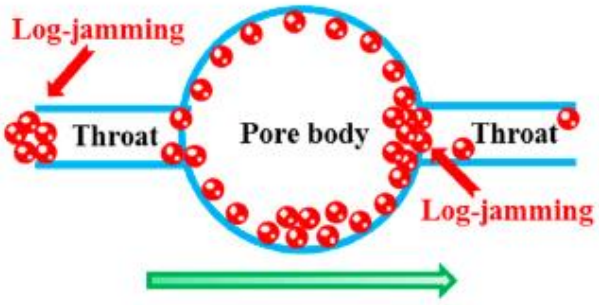

Figure 2.8: Schematic of pore clogging caused by log-jamming (Sun et al. 2017)

2.4 Colloids Transport in Saturated Porous Media

Auset and Keller (2004) conducted experiments to investigate the particle transport behavior in porous media. They used polydimethylsilxane (PDMS) to create several micro-models to represent porous media. The models are demonstrated in **Fig 2.9**. In general, the pattern for those microscope models are quadrilateral network of 100 pore bodies with 60 μm diameter. **Fig. 2.9 (a), (b)** and **(c)** present networks with channel width of 10 μm, 20 μm, as well as combined 10 and 20 μm, respectively.

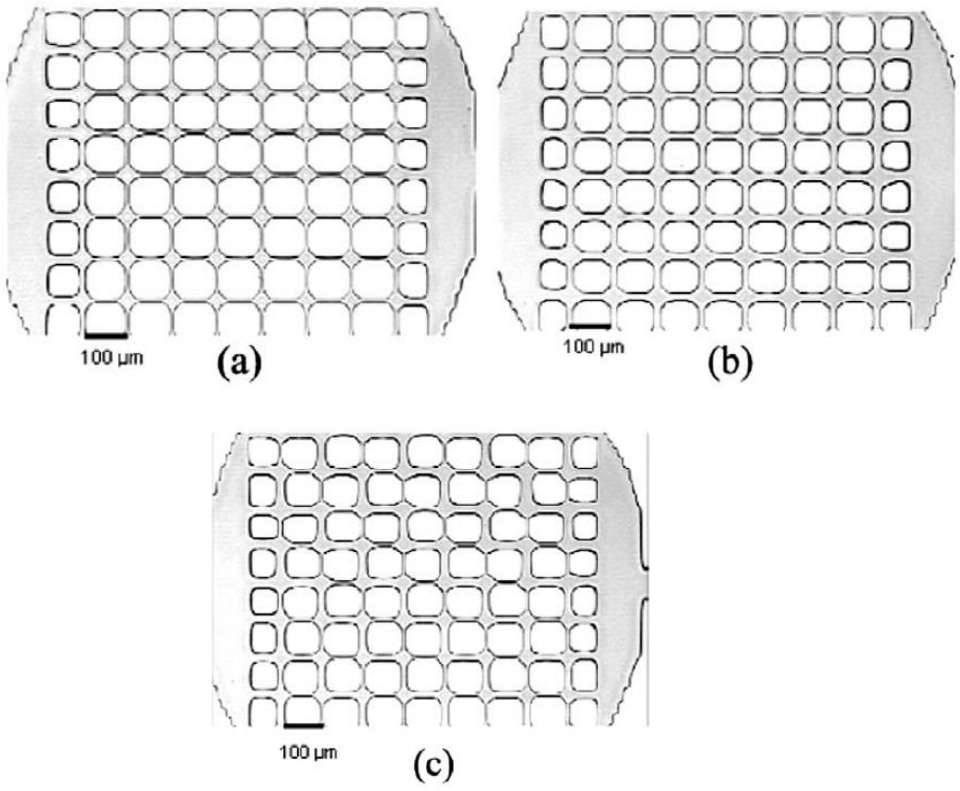

Figure 2.9: Optic microscope images of the polymer replica containing channel patterns with three different channel widths. (Auset and Keller, 2004)

They injected four sizes of microspherical paticles with 2, 3, 5, and 7 μm in diameter into the porous media that fully saturated with water. The particle trajectories were obtained and the results for 3 μm diameter case is demonstrated in **Fig. 2.10**. The picture on left illustrates several randomly chosen trajectories in the pore network with channel width of 20 μm (regular). The picture on the right demonstrates trajectories in combined 10 and 20 μm channel width pore network (irregular). It had been observed that particles took more detours in irregular pore network because of the more complex structure.

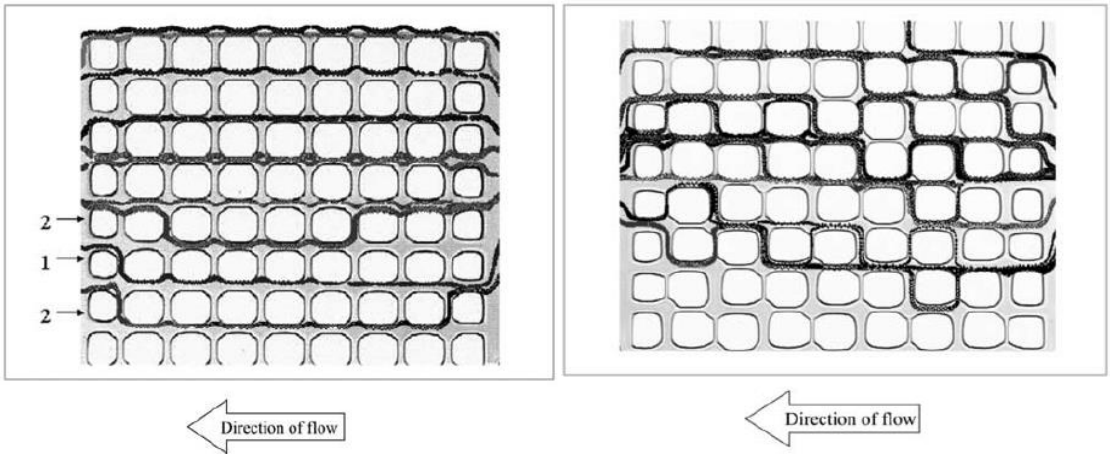

Figure 2.10: Trajectories of 3 μm particles. Picture on the left is for regular shaped channel, and the right one is for irregular shaped channel. (Auset and Keller, 2004)

In addition, they observed that those particles travel in the center streamlines have low possibility to detour. In terms of particle size, larger particles are more likely to travel in the center part of the flow, therefore, they preferentially flow in straighter pathways. However, smaller particles are more likely to detour from straighter pathways because they always travel near the pore wall. Therefore, the dispersion of colloids depends on both flow path geometry and colloid size.

Sirivithayapakorn and Keller (2003) also investigated the pore size exclusion effect during colloid transport process. The pore size exclusion effect is a phenomenon that the colloids are restricted to flow in high velocity streamlines in large pores. They used pore scale micro model that made of a thin slice of fine sand. The imaged and digitized picture of the porous media is demonstrated in **Fig. 2.11**. The size of the image is approximately 509×509 μm. The pore throats are between 3 to 20 μm in diameter. The colloid size that they used were 0.05, 1, 2, and 3 μm. Three different pressure were set for the experiment.

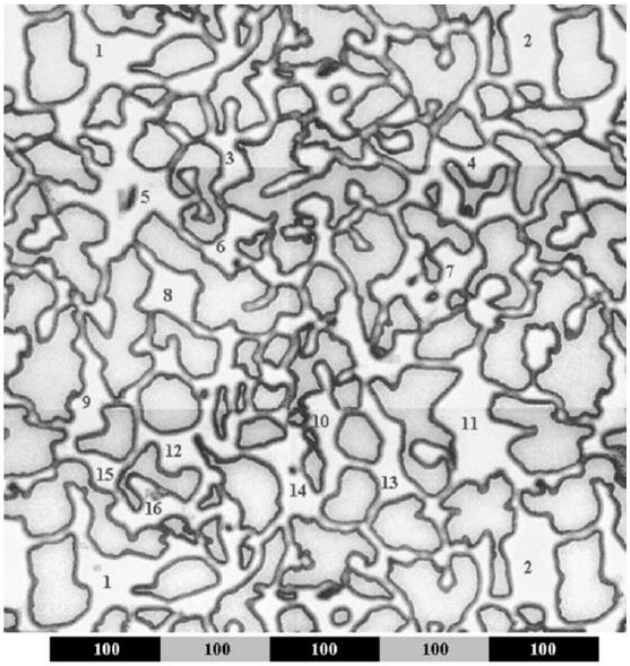

Figure 2.11: Composite image of pore network (Sirivithayapakorn and Keller, 2003).

They observed that at high pressure, large colloids only flowed through large pore throats. At low pressure, large colloid could flow to other large pores. In contrast, small colloids were more likely flow into small pore throats. In addition, it had been discovered

that 3 μm colloids flowed into different pore throats at different pressures, which is an evidence of size exclusion effect. The preferential paths for different colloids are depicted in **Fig 2.12**. The 0.05 μm colloids had the most pathways, which indicates highest particle dispersion. It can be explained that small particle can be easier to move through wide range of pores in comparison to large particle.

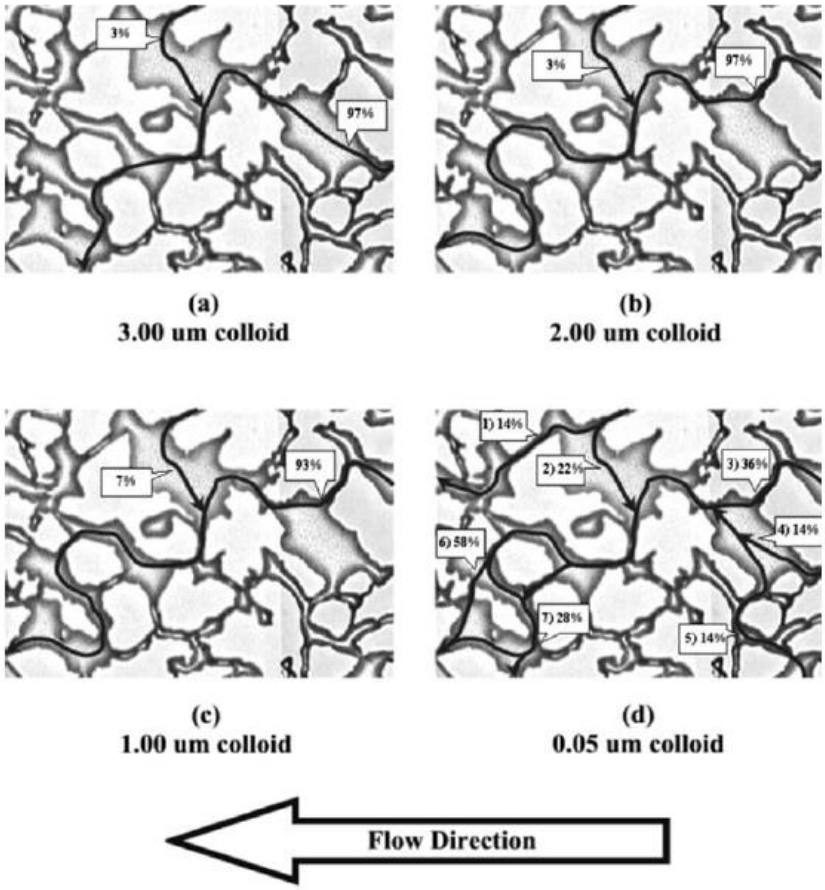

Figure 2.12: Trajectories of colloids with different diameters (Sirivithayapakorn and Keller, 2003).

2.4 Solving Particle Transport Problem Using CFD Technique

When addressing the issue of large-scale proppant transportation in fractures, petroleum engineers rely on two methods: (1) the velocity model saying that viscosity produce the influence of the proppant load on the fluid, and (2) the mixed phase model in which the proppant and fluid are considered as different phases with different velocities (Roy et al. 2015). The first model is not sophisticated because it only applicable for high viscosity fluids, and it cannot describe the correct particle behavior in low viscosity fluid. The reason is that proppant transport behavior will be affected by the friction with the fracture surface, particle jamming, and proppant pack formation, which result in the velocity difference between proppant and fluid. The second model (mixed phase model) tracks particle and fluid separately, therefore, it can capture the complex behavior between them.

There are two computational fluid dynamic (CFD) approaches that treat particle and fluid separately when dealing with transport problem in hydraulic fracture or porous media. The first one is called Lagrangian approach, also referred to as particle tracking method or Discrete Phase Model (DPM) (Kong et al. 2016). This method treats the fluid as a continuum phase by solving the Navier- Stokes (N-S) equation, and then tracks each particle as discrete phase by coupling them with the flow field. The limitation of this method is the volume of disperse phase cannot employed because DPM assumes particle loading is low compared with whole domain and particle-particle interaction is not being considered. However, if DPM is coupled with DEM (Disperse Element Method), the particle-particle and particle-wall interactions can be captured. DEM is the method of

applying Newton's law to particles to obtain their motions. The second method is the Euler-Euler approach, which treats each phase as an interpenetrating continuous phase. It solves a set of momentum and mass balance equations for both solid and liquid phase. Solid phase is considered as continuum fluid phase of particle. The Euler-Euler model is the most complex and computationally intensive among the multiphase models.

Tong and Mohanty (2016) introduced a Dense Discrete Phase Model (DDPM), which is the combination of the two approaches mentioned above. The difference between DDPM and the other two models is that the solid particle phase is tracked by Lagrangian approach, and then mapped back to Eulerian grid. The advantage of this method is that particles are regarded as parcel groups, therefore computation can be reduced.

2.5 Meshing in Finite Element Method

Finite element method (FEM) is one of the most common methods to solve partial differential equations that engineers use to model physical behaviors (Haaland. 2016). In finite element analysis, meshing generation enables a model being divided into finite number of elements with certain number of node points. The calculation is completed at those limited number of node points and then interpolate the results for the entire model domain.

The mesh shape and size in FEM highly affects the accuracy of the calculation. In COMSOL Multiphysic, meshing utilizes four different element types: tetrahedra (tets), hexahedra (bricks), triangular prisms (prisms), and pyramids. Those shapes can be seen below as **Fig 2.13**.

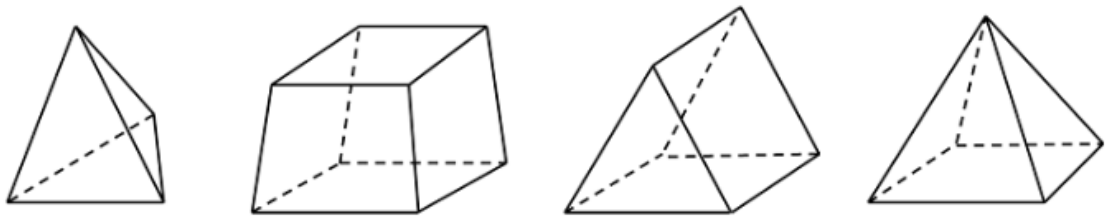

Figure 2.13: Image of different element types (Haaland. 2016).

Haaland used COMSOL to model two drilling fluid behavior in the well. The model that he built was a 2-D pipe that contained two drilling fluids. He used free triangular elements with three different sizes for mesh generation in COMSOL. At the interface part of the model, a finer mesh was generated and more elements where distributed near that area. As for the model boundary, elements were coarser distributed. For the rest domain of the model, an extremely coarse mesh was generated. Since the expected results could mainly be obtained at the interface part of the model, finer mesh was implemented. Choosing different sizes of mesh based on model requirement can reduce the total number of elements and finally reduce the computational cost.

Chapter 3: Methodology

3.1 Simulation Software

The simulation software that used in this thesis is COMSOL Multiphysics® (also refer to as COMSOL). It is a finite element analysis simulator which can be used to deal with coupled multiple physics problem. The two interfaces that were implemented in this thesis are computational fluid dynamic (CFD) module and particle tracing module.

In CFD module, the laminar flow and creeping flow interfaces were used to model steady state flow at relatively low Reynolds number for Newtonian fluids. The velocity field can be calculated by solving Navier-Stokes equation.

Particle tracing module were used to model Euler-Lagrange multiphase flow problem, where particles or droplets are considered as rigid particles. The interaction between particle and fluid were obtained by coupling the CFD interface with particle tracing interface.

3.2 Model Assumptions

In all simulations, fluid velocities were calculated assuming that particle does not affect fluid properties. Next, calculated fluid velocity values were used to determine particle velocity as a function of time and space. The major assumptions of this study are as follow:

1. Incompressible flow
2. Laminar Darcy fluid flow
3. No particle-particle interaction is considered
4. Fluid properties are not affected by particle flow

5. No slip boundary condition at the wall
6. All particles are naturally buoyant; drag force is the dominant factor

3.3 Governing Equation for Particle Transport in Fluid Flow

To model laminar flow in the tube, the CFD module was implemented. The governing equations solved for incompressible fluid flow are as follow:

$$\rho\frac{\partial u}{\partial t}+\rho(u\cdot\nabla)u=\nabla\cdot\left[-pI+\mu\left(\nabla u+(\nabla u)^{T}\right)\right]+F$$
$$\rho\nabla\cdot(u)=0 \tag{3.1}$$

where ρ is fluid density, u is the fluid velocity, μ is fluid viscosity and F is additional forces acting on fluid.

Once the flow interface being calculated, the Particle Tracing module was added to model particulate flow. In this model, it is assumed that all particles are naturally buoyant; therefore, the gravity and buoyancy forces can be ignored and the drag force (F_D) is the dominant factor in determining the particle trajectories. The governing equation for particle motion is

$$\frac{d(m_p v)}{dt}=F_D \tag{3.2}$$

where u is fluid velocity and v is particle velocity, m_P is the mass of the particle, and F_D is drag force. The initial velocity of particles was set same as the initial velocity of fluid flow. In general drag force can be defined as:

$$F_D=\frac{1}{\tau_p}m_p(u-v) \tag{3.3}$$

where τ_P is relaxation time and can be expressed as:

$$\tau_p = \frac{4}{3}\frac{\rho_p d_p}{\rho C_D |u - v|} \tag{3.4}$$

where ρ_P is particle density, d_P is particle diameter, and C_D is drag force coefficient. The appropriate formulation of C_D, depends on the relative Reynolds number (Re_r) of the particle in the fluid. For a spherical particle the relative Reynolds number is:

$$\mathrm{Re}_r = \frac{\rho |u - v| d_p}{\mu} \tag{3.5}$$

Based on Stokes drag law, for $Re_r \ll 1$, the drag force coefficient, C_D can be estimated as:

$$C_D = \frac{24}{\mathrm{Re}_r} \tag{3.6}$$

Combining **Eqs. 3.4-3.6**, the particle relaxation time yields to be:

$$\tau_p = \frac{\rho_p d_p{}^2}{18\mu} \tag{3.7}$$

To model the velocity difference between particle and fluid, the NE effect is defined as a function of particle velocity and local fluid velocity, which can be written as

$$NE = 1 - \frac{u}{v} \tag{3.8}$$

3.4 Adapt Harmonic Oscillator Equation to Describe NE Effects

Viscous damping occurs when the damping force generated is proportional to the velocity of the particles. One way that viscous damping arises in jarring analysis is from the interaction of a solid and liquid at their interface (Lake. 2006).

In particulate flow system, particle and its carrier fluid have interaction at their interface. In order to describe the non-equilibrium (NE) effects between particle and fluid, harmonic oscillator equation is carried out.

In mechanical vibration system, the harmonic oscillator equation with damping is driven by solving Newton's second law equation, which is

$$\frac{d^2x}{dt^2} + 2\zeta\omega_0 \frac{dx}{dt} + \omega_0{}^2 x = 0 \tag{3.9}$$

where

$\omega_0 = \sqrt{\frac{k}{m}}$ is called the un-damped angular frequency of the oscillator,

$\zeta = \frac{c}{2\sqrt{mk}}$ is called the damping ratio.

The system behavior depends on the value of damping ratio (ζ).

- Over-damped ($\zeta > 1$): The system returns to steady state without oscillating. Larger values of the damping ratio ζ return to equilibrium more slowly.
- Critically damped ($\zeta = 1$): The system returns to steady state as quickly as possible without oscillating
- Underdamped ($\zeta < 1$): The system oscillates with the amplitude gradually decreasing to zero.

If $\zeta > 1$, an imaginary number is involved when solving **Eq. 3.8**. Also, $\zeta > 1$ implies that the system returns the equilibrium state without oscillation. Therefore, it is not a good approach to explain the NE behavior. In order to have a specific equation to describe the NE, the underdamped behavior ($\zeta < 1$) will be applied to describe the vibration behavior

between particle velocity and fluid. The general solution of **Eq. 3.9** for $\zeta < 1$ can be written as

$$x(t) = Ae^{-\zeta\omega_0 t}\sin\left(\sqrt{1-\zeta^2}\,\omega_0 t + \varphi\right) \tag{3.10}$$

The NE effect parameter is proposed to be

$$NE = 1 - \frac{v_p}{v_f} = Ae^{-\zeta\omega_0 t}\sin\left(\sqrt{1-\zeta^2}\,\omega_0 t + \varphi\right) \tag{3.11}$$

where A is oscillation amplitude, ζ is damping ratio. In this thesis, it is hypothesized that A represents the magnitude of NE and ζ represents time needed to attain equilibrium. High amplitude implies large NE between particle and fluid, whereas low damping ratio indicates the particle need long time to get equilibrium with its carrier fluid.

3.5 Curve Fitting Using MATLAB®

MATLAB codes were designed to match the harmonic oscillation equation with the simulation data. For curve fitting, the equation that used is

$$y = ae^{-bx}\sin\left(cx + d\right) \tag{3.11}$$

Once all the coefficients (a, b, c, and d) are obtained, the ζ and ω_0 can be determined by

$$\zeta = \frac{b}{\sqrt{b^2 + c^2}} \tag{3.12}$$

$$\omega_0 = \sqrt{b^2 + c^2} \tag{3.13}$$

Chapter 4: Non-Equilibrium Effects in Straight and Periodic Converging-Diverging Tubes

4.1 Straight Tube Model

4.1.1 Model Set Up

The basic geometry schematic of the straight tube model can be seen below as **Fig 4.1**. A straight tube with a uniform radius of 100 μm and a total length of 250 μm was modeled. In order to reduce computational cost, the geometry was cut to a quarter of the original tube along the symmetry line.

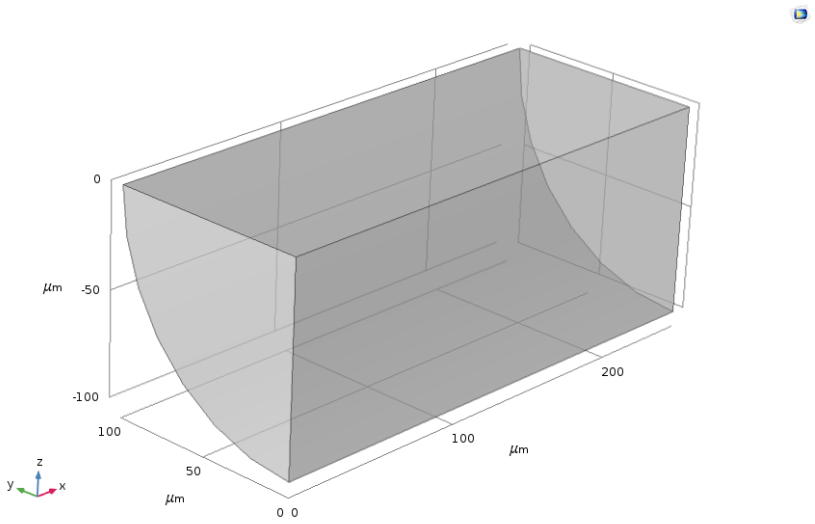

Figure 4.1: Basic schematic of straight tube generated in COMSOL.

Fluid was given a velocity of 0.004 m/s at the inlet boundary. The outlet boundary was set as p=0 refer to inlet boundary. Particles with different diameters were injected from different positions at inlet boundary to outlet boundary for different cases (each case had identical particle diameter). The details of the simulation model are listed in **Table 4.1**.

Table 4.1: Simulation inputs for straight tube model

Parameter	Value	Unit
Fluid density	750	kg/m^3
Fluid viscosity	0.5, 1, 3, 5	cp
Initial velocity	0.004	m/s
Particle diameter	25	μm
Particle density	2000	kg/m^3

Mesh independent study was performed with different mesh sizes. The meshing result is shown in **Fig 4.2**. The final mesh that being used in the simulation was free tetrahedral shape with a maximum element size of 3 μm and a minimum element size of 1 μm. The reason why tetrahedral shape is chosen is because it can be easily generated to be conforming where adjacent elements share a whole edge or a whole face (Ho-Le. 1988).

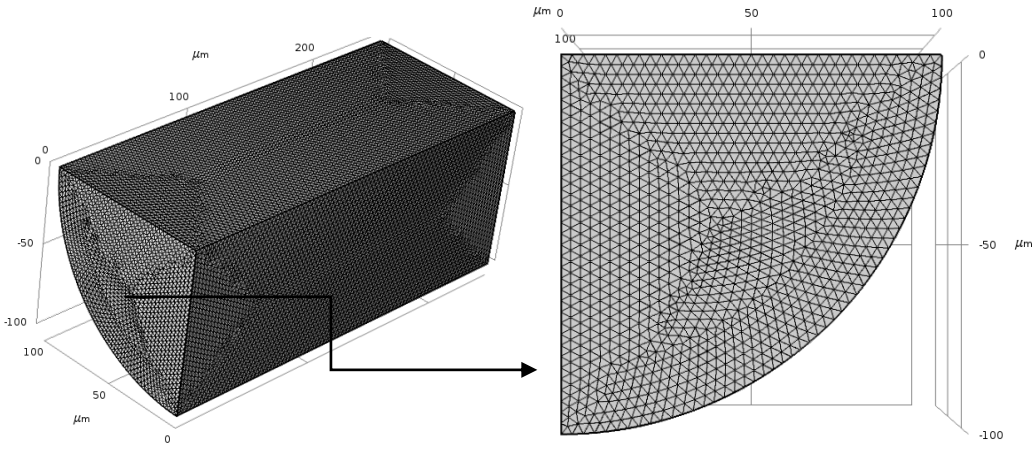

Figure 4.2: Mesh generation with tetrahedral shape.

4.1.2 Fluid Velocity Profile and Particle Trajectory

The velocity profile of μ = 1 cp case is illustrated in **Fig 4.3**. The flow velocity distribution across the tube follows the character of Poiseuille flow. The maximum velocity, which is approximately 0.006 m/s occurs at the center of the tube, and the velocity at the flow boundary is equal to zero.

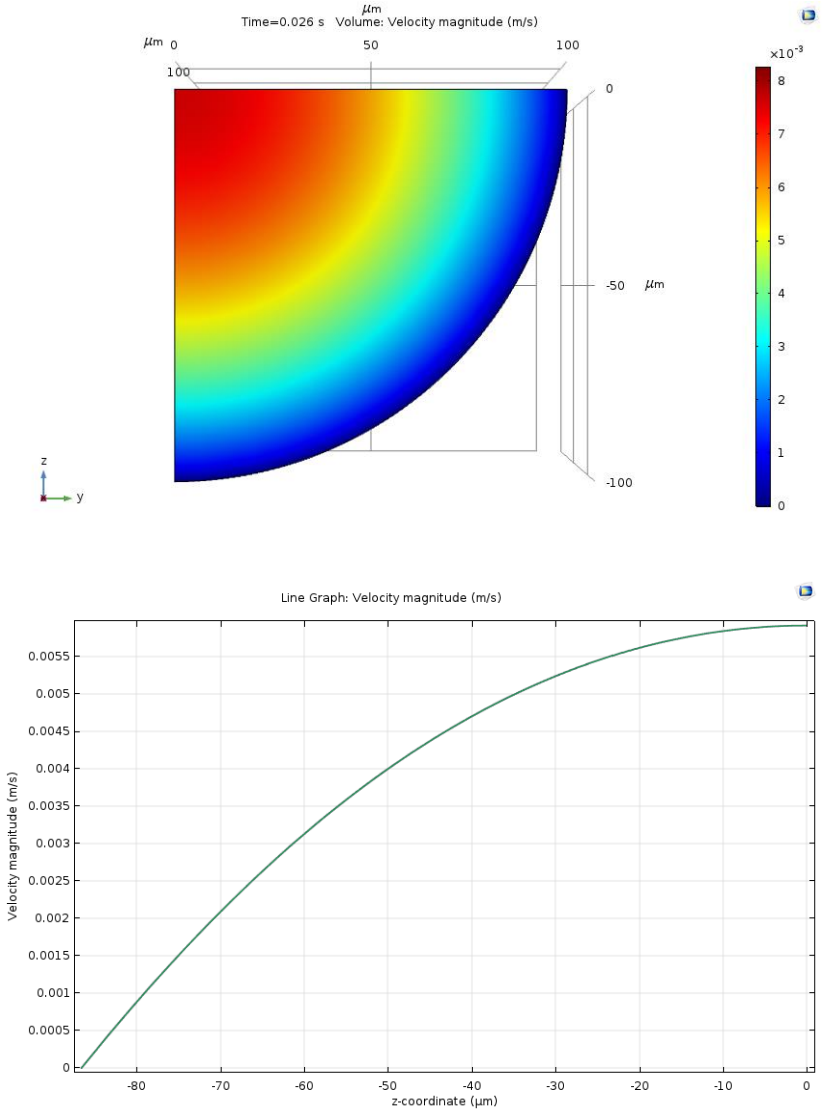

Figure 4.3: Velocity profiles in the cross section (top) and along the z-axis (bottom).

Using Hagen-Poiseuille Law, the fluid velocity at any given radius (r) inside the tube can be express as **Eq. 4.1**.

$$v_f(r) = v_{\max}\left[1-\left(\frac{r}{R}\right)^2\right] \tag{4.1}$$

where v_{max} is the maximum fluid velocity inside the tube, and R is the radius of the tube. In this case v_{max} is around 0.006 m/s, and R equals 100 μm (0.0001m). Plugging them into **Eq. 4.1**, the velocity distribution inside tube yields to be

$$v_f(r) = 0.006\left[1-\left(\frac{r}{1\times10^{-4}}\right)^2\right] \tag{4.2}$$

The particle trajectory is shown in **Fig 4.4**. With only drag force, particles are affected by the velocity field generated by fluid flow, so they move along the flow stream line. Therefore, particles at the center part of the tube have high velocities.

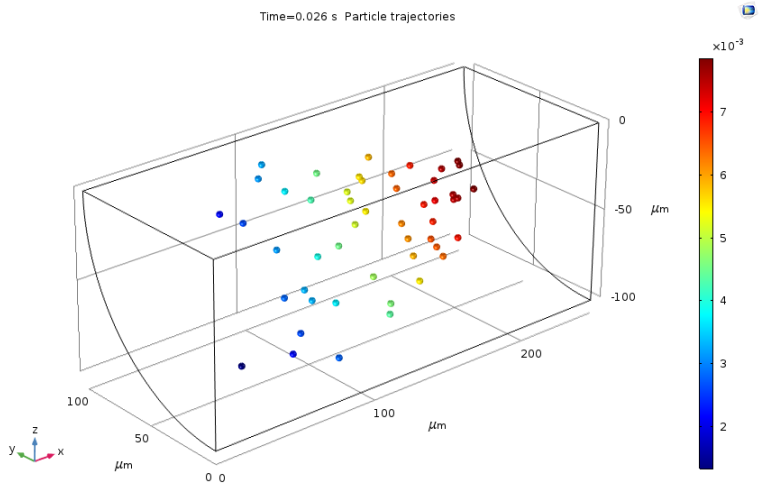

Figure 4.4: Particle trajectories inside the tube. Color scale represents the magnitude of particle velocities.

4.1.3 Non-Equilibrium Parameter Determination

The NE parameter $(1 - \frac{v_p}{v_f})$ was evaluated within COMSOL. Simulation results were matched with harmonic oscillator equation to obtain the magnitude (A) and damping ratio (ζ) values. P10, P50, and P90 values on cumulative distribution functions (CDF) of A and ζ were recorded separately. P50 was used to represent the most likely value, whereas P10 and P90 were used to determine uncertainty.

For the fluid viscosity of 1cp, the NE parameter as a function of time for one of the 50 particles is plotted in **Fig 4.5**. During early stage (when particle is just injected into the tube), there is velocity difference between particle and fluid. In that time period, particle velocity is always less than fluid velocity. After a certain time, particle and fluid reach same velocity, which can be described as equilibrium state.

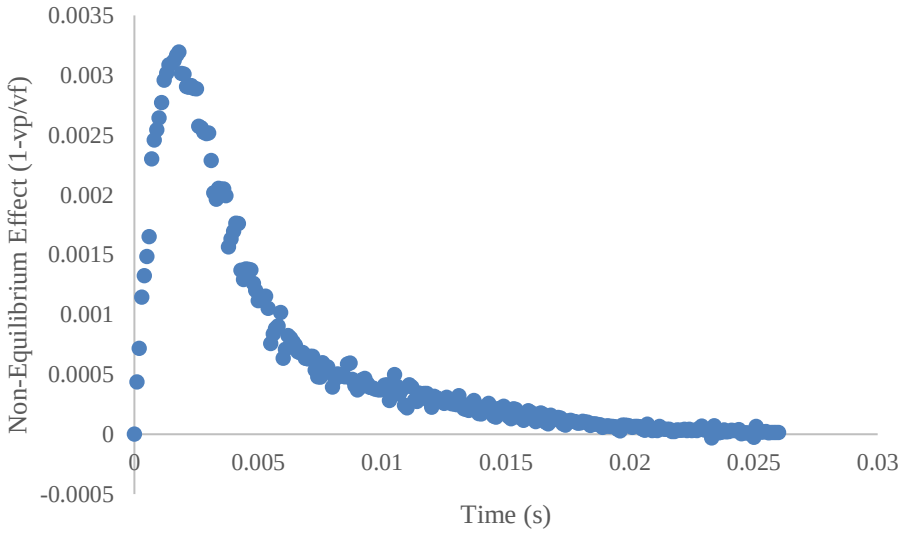

Figure 4.5: NE parameter as a function of time solved with COMSOL.

To model the NE, the adapted harmonic oscillation equation (**Eq. 3.11**) was implemented to match with simulation results. A perfect match with R^2 =0.98 was obtained and it can be seen in **Fig 4.6**.

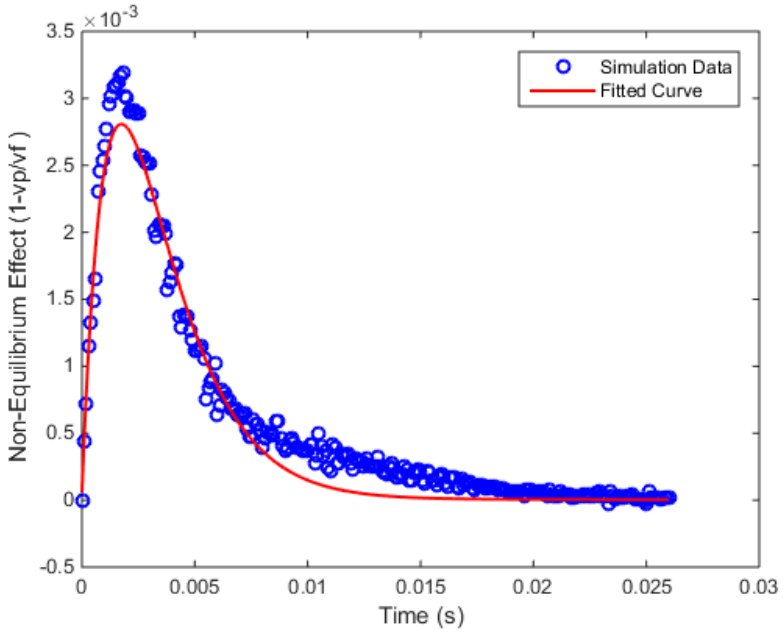

Figure 4.6: Curve fitting for single particle with MATLAB.

Same curve fitting process was performed for all 50 particles. The statistic results for two key factors of NE, A and ζ are presented in **Fig 4.7**. The P50 values of A and ζ at their cumulative distribution function are 0.025 and 0.977, respectively.

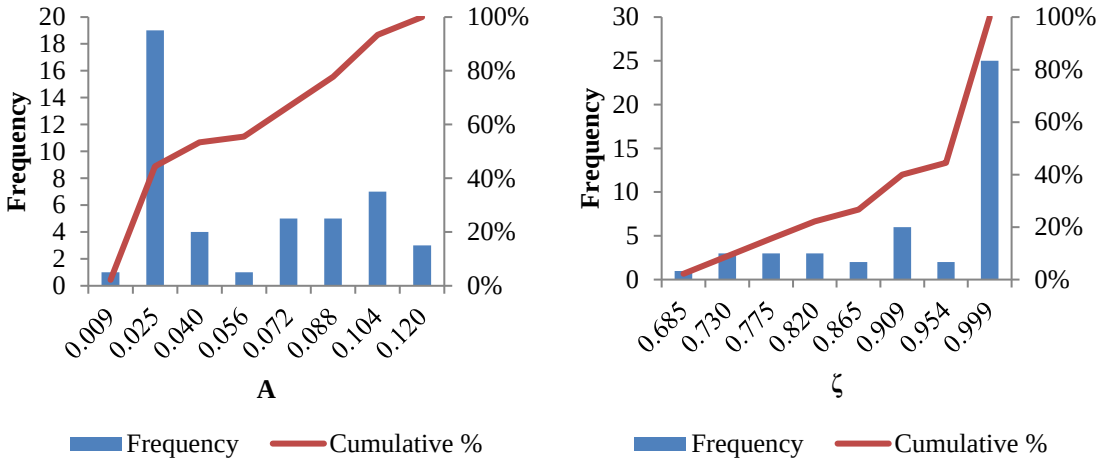

Figure 4.7: Histograms and CDFs of A and ζ values obtained from curve fitting for case of $\mu = 1$ cp.

4.1.4 Decouple Particle Equation from Fluid Equation

The ω_0 and φ values were also determined by using P50 value on their cumulative distribution functions. All coefficients in the harmonic oscillation equation were obtained and they are listed in **Table 2.2**.

Table 4.2: Coefficients of harmonic oscillation equation for straight tube obtained from curve fitting

Coefficient	P50	P10	P90
A	0.025	0.009	0.104
ζ	0.977	0.73	0.999
ω_0	305	245	780
φ	100	100	100

Plug the P50 values of those coefficients into **Eq 3.11**, the equation yields to be

$$1-\frac{v_p}{v_f} = 0.025e^{-298t}\sin\left(66t+100\right) \tag{4.3}$$

Combine **Eq. 4.2** with **Eq. 4.3**, the particle velocity for any given radius (r) and time (t) for the case of $\mu = 1$ cp is determined to be

$$v_p(r,t) = 0.006\left[1-\left(\frac{r}{1\times10^{-4}}\right)^2\right]\left[1-0.025e^{-298t}\sin\left(66t+100\right)\right] \tag{4.4}$$

4.1.5 Sensitivity Analysis

Sensitivity analysis was performed on fluid viscosity to investigate how fluid viscosity affect NE parameters. Pure dodecane and Earlsboro crude whose viscosities are 1.34 cp and 4.6 cp were used in EOR experiment (Wang et al. 2018). Simulations were built for cases of $\mu = 5$ cp, 3cp and 0.5 cp. Other inputs were kept same with previous case. The histograms and cumulative distribution functions for A and ζ values are presented in **Figs 4.8-4.10**

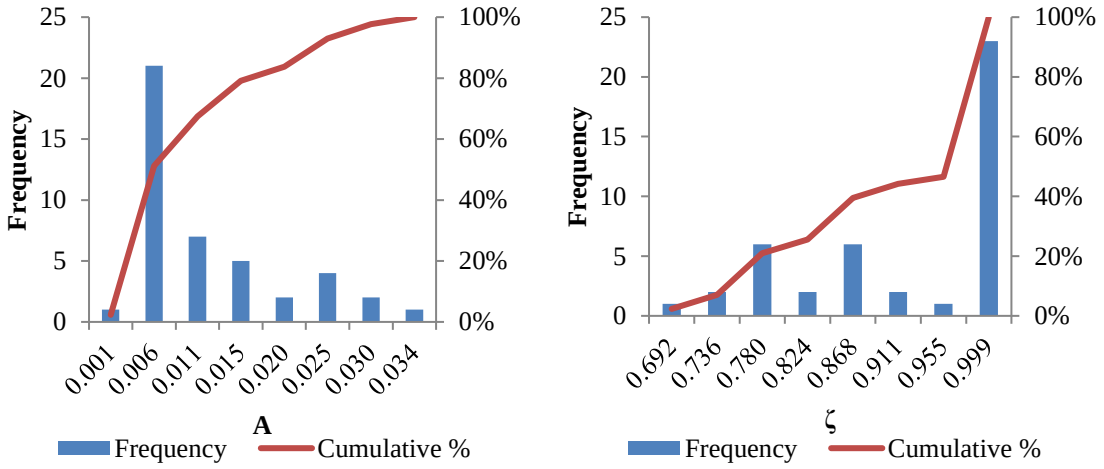

Figure 4.8: Histograms and CDFs of A and ζ values obtained from curve fitting for case of $\mu = 5$ cp.

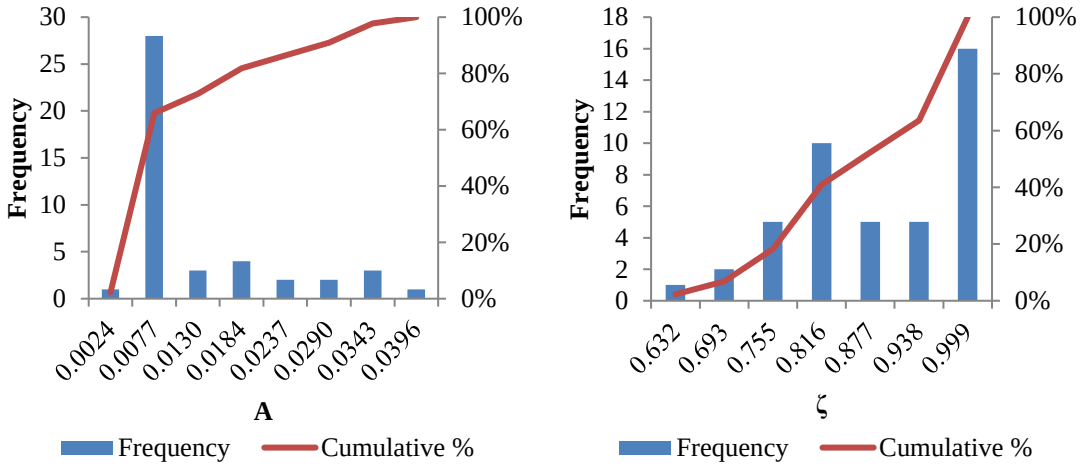

Figure 4.9: Histograms and CDFs of A and ζ values obtained from curve fitting for case of $\mu = 3$ cp.

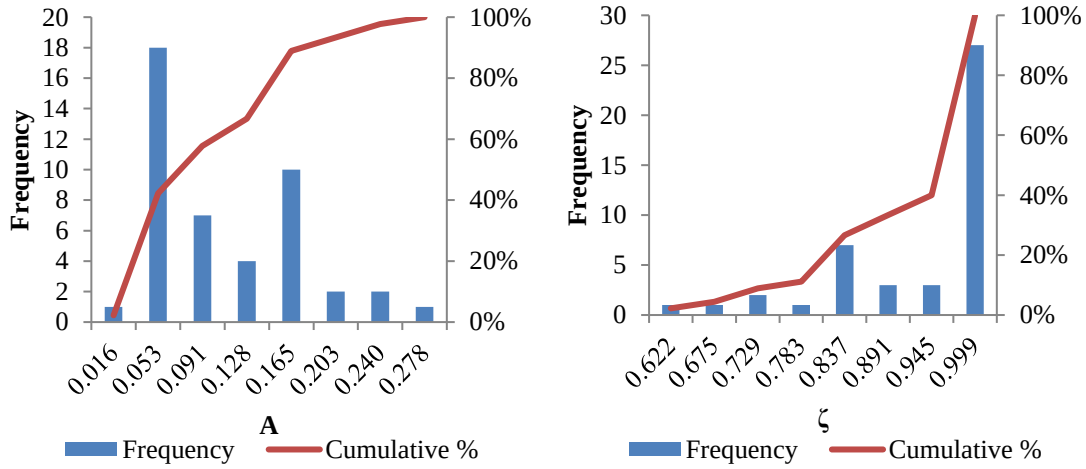

Figure 4.10: Histograms and CDFs of A and ζ values obtained from curve fitting for case of $\mu = 0.5$ cp.

P50 values of A and ζ for cases of $\mu = 5\text{cp}, 3\text{ cp}, 1\text{cp}$ and 0.5 cp are plotted in **Fig 4.11**. It can be observed that a high fluid viscosity value yields a low magnitude of NE between particle and fluid. High viscosity fluid makes particle and fluid get equilibrium state quickly compared with low viscosity fluid. The damping ratios (ζ) for all cases are

close to 1, which indicates that particles and fluid will reach equilibrium states as quick as possible in straight tube with uniform radius.

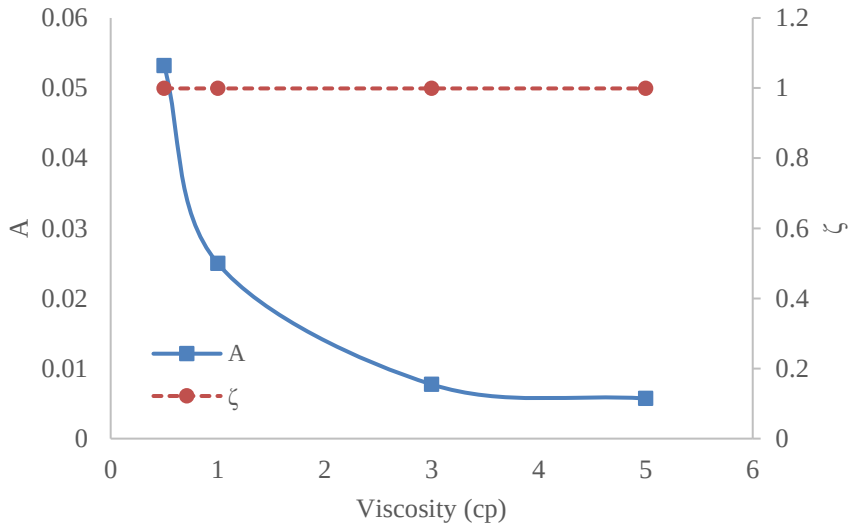

Figure 4.11: Comparisons of A and ζ values at different fluid viscosities.

4.2 Periodic Converging-Diverging Tube Model

4.2.1 Model Set Up

The basic schematic of the converging-diverging shaped tube model is demonstrated in **Fig 4.12**. Two diverging shaped tubes and one converging shaped tube connect with each other. Each tube has a maximum radius of 100 μm and a minimum radius of 50 μm as well as a tube length of 250 μm.

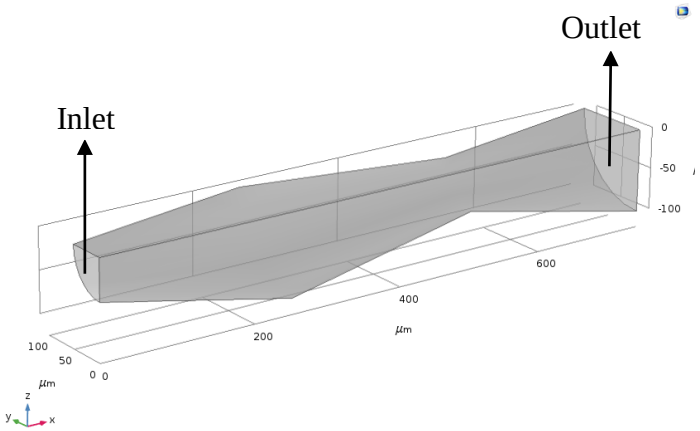

Figure 4.12: Basic schematic of periodic converging-diverging tube generated in COMSOL.

Particles were injected at the same velocity with the initial fluid velocity from the inlet boundary to outlet boundary. The details of the simulation are listed in **Table. 4.3**.

Table 4.3: Simulation inputs for periodic converging-diverging model

Parameter	Value	Unit
Fluid Density	750	kg/m^3
Fluid Viscosity	0.5, 1, 4	cp
Initial Velocity	0.008	m/s
Particle Diameter	25	μm
Particle Density	2000	kg/m^3

4.2.2 Fluid Velocity Profile and Particle Trajectory

The velocity profile of $\mu = 1$ cp case is illustrated in **Fig 4.13**. Similar to tube with uniform radius, the velocity distribution in periodic converging-diverging tube follows the character of Poiseuille flow. Fluid velocity magnitude is higher in small radius region compared with that of big radius region.

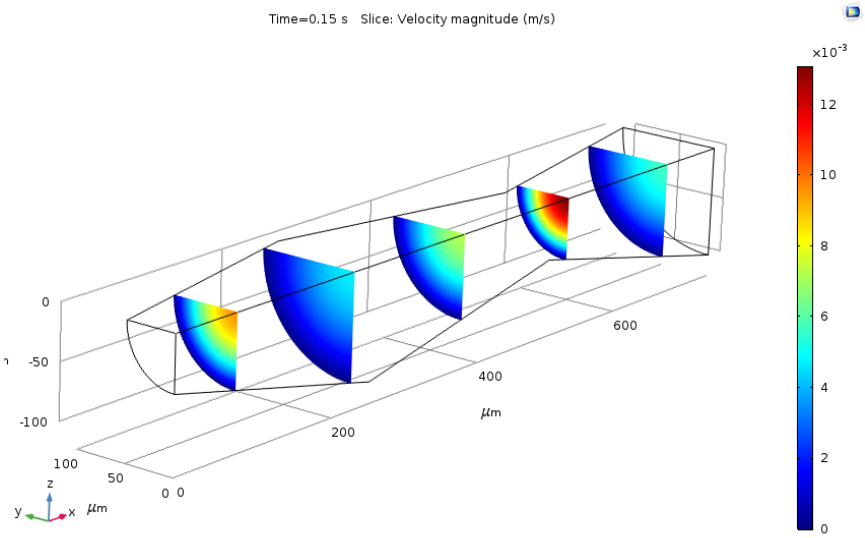

Figure 4.13: Fluid velocity distribution inside the periodic converging-diverging tube.

The velocity distributions along the z-axis for cross-sections with maximum and minimum radii were evaluated in COMSOL and they can be seen below as Fig. For the cross-sections with radius of 100 μm and 50 μm, the maximum velocities are approximately 0.0045 m/s and 0.014 m/s, respectively.

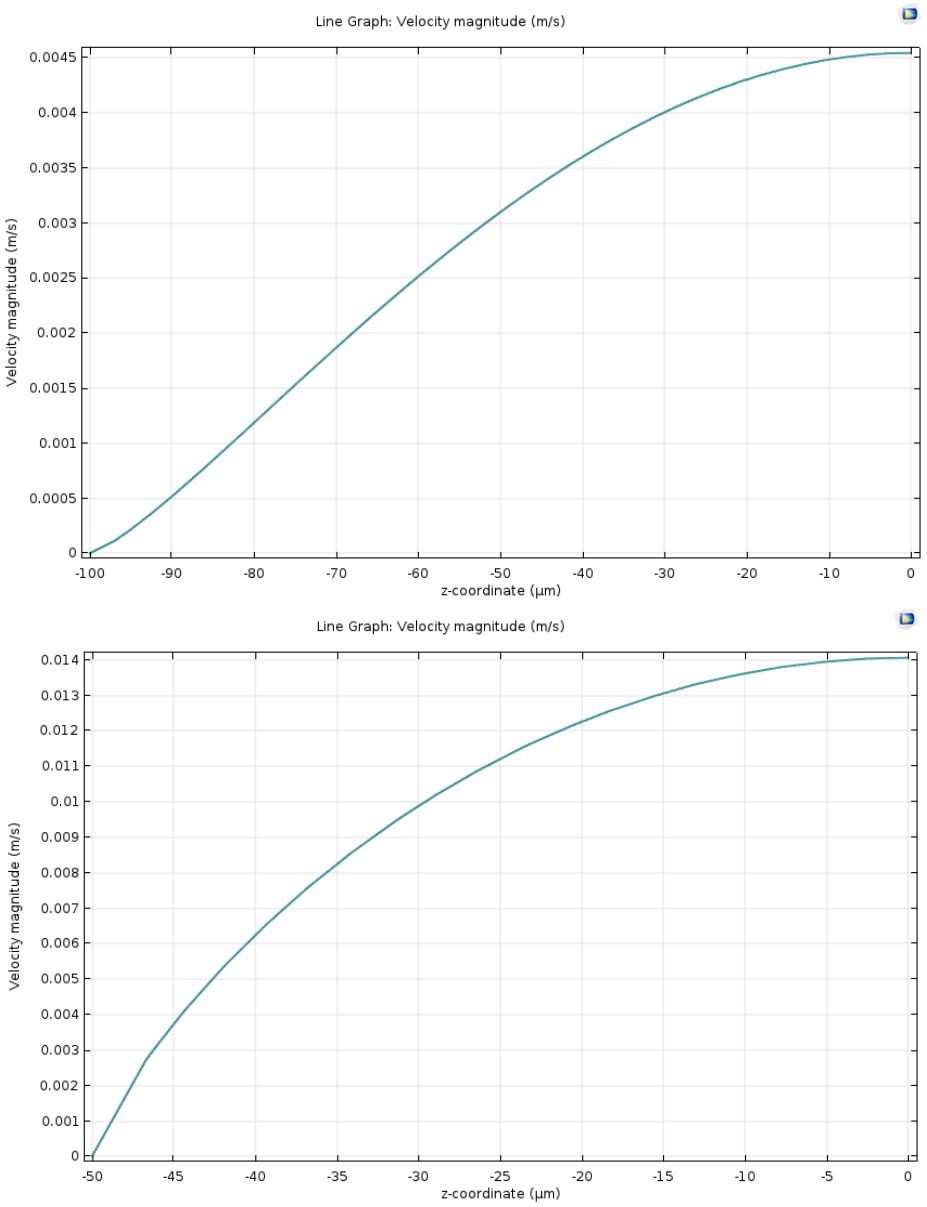

Figure 4.14: Velocity distributions along the z-axis in maximum cross-section (top) and minimum cross-section (bottom).

The velocity profile $v(r,z)$ in a tube whose cross-section area is gradually changing with the distance along the flow direction remains parabolic (Bahrami et al. 2008). The schematic velocity profile can be seen below as **Fig 4.15**.

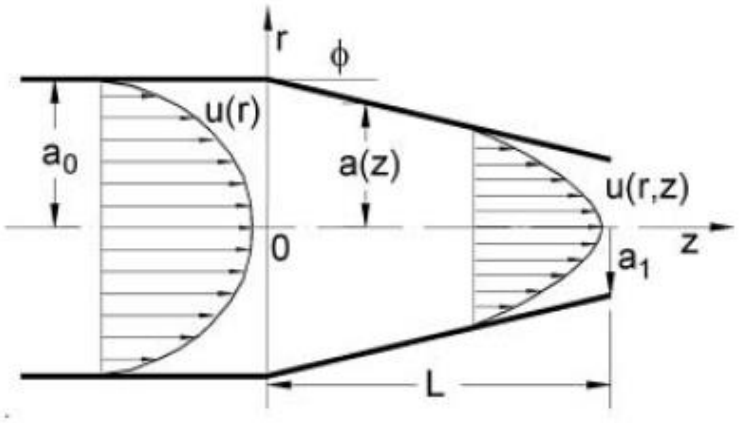

Figure 4.15: Schematic of varying cross-section tube (Bahrami et al. 2008).

Therefore, the axial velocity needs to be described as

$$u(r,z) = 2u_m(z)\left[1-\left(\frac{r}{a(z)}\right)^2\right] \tag{4.5}$$

where $u_m(z)$ is the average velocity at the axial location z, $a(z)$ is the tube radius at location z. By applying conservation of mass

$$u_m(z) = \left[\frac{a_0}{a(z)}\right]^2 u_{m,0} \tag{4.6}$$

where a_0 is the tube radius at initial point. Combining **Eq. 4.5** and **Eq. 4.6**, the axial velocity equation yields to be

$$u(r,z) = 2u_{m,0}\left[\frac{a_0}{a(z)}\right]^2\left[1-\left(\frac{r}{a(z)}\right)^2\right] \tag{4.7}$$

For a convergent shaped tube,

$$a(z) = R_{\min} + \frac{L-z}{L}\left(R_{\max} - R_{\min}\right) \tag{4.8}$$

where R_{min}, R_{max} and L are the minimum tube radius, maximum tube radius, and tube length respectively.

Similar for a divergent shaped tube,

$$a(z) = R_{\min} + \frac{z}{L}\left(R_{\max} - R_{\min}\right) \tag{4.9}$$

Combining **Eq. 4.7** with **Eq. 4.8**, we get the generalized velocity equation in a converging tube, which is

$$u(r,z) = 2u_{m,0}\left[\frac{a_0}{R_{\min} + \frac{L-z}{L}\left(R_{\max} - R_{\min}\right)}\right]^2\left[1 - \left(\frac{r}{R_{\min} + \frac{L-z}{L}\left(R_{\max} - R_{\min}\right)}\right)^2\right] \tag{4.10}$$

Combining **Eq. 4.7** with **Eq. 4.9**, we can get the generalized velocity equation in a diverging tube, which is

$$u(r,z) = 2u_{m,0}\left[\frac{a_0}{R_{\min} + \frac{z}{L}\left(R_{\max} - R_{\min}\right)}\right]^2\left[1 - \left(\frac{r}{R_{\min} + \frac{z}{L}\left(R_{\max} - R_{\min}\right)}\right)^2\right] \tag{4.11}$$

Plug $\mathrm{R_{min}} = 5 \times 10^{-5}$ m, $\mathrm{R_{max}} = 1 \times 10^{-4}$ m, $\mathrm{L} = 2.5 \times 10^{-4}$ m, and $2u_{m,0}$=0.0045 m/s into **Eq. 4.10**, the fluid equation for any given radius (r) and axial length (z) inside the convergent tube yields to be

$$v_f(r,z) = 4.5\times10^{-3}\left[\frac{1\times10^{-4}}{1\times10^{-4} - \frac{z}{5}}\right]^2\left[1 - \left(\frac{r}{1\times10^{-4} - \frac{z}{5}}\right)^2\right] \tag{4.12}$$

Plug $2u_{m,0}$=0.014 m/s into **Eq. 4.11**, the particle equation for any given radius (r) and axial length (z) inside the divergent tube yields to be

$$v_f(r,z) = 0.014\left[\frac{5\times10^{-5}}{5\times10^{-5}+\frac{z}{5}}\right]^2\left[1-\left(\frac{r}{5\times10^{-5}+\frac{z}{5}}\right)^2\right] \tag{4.13}$$

The particle trajectories in periodic converging-diverging tube is demonstrated in **Fig 4.16**. The particle motions were only affected by the fluid flow field, therefore, high velocity is be observed at the tube with small radius.

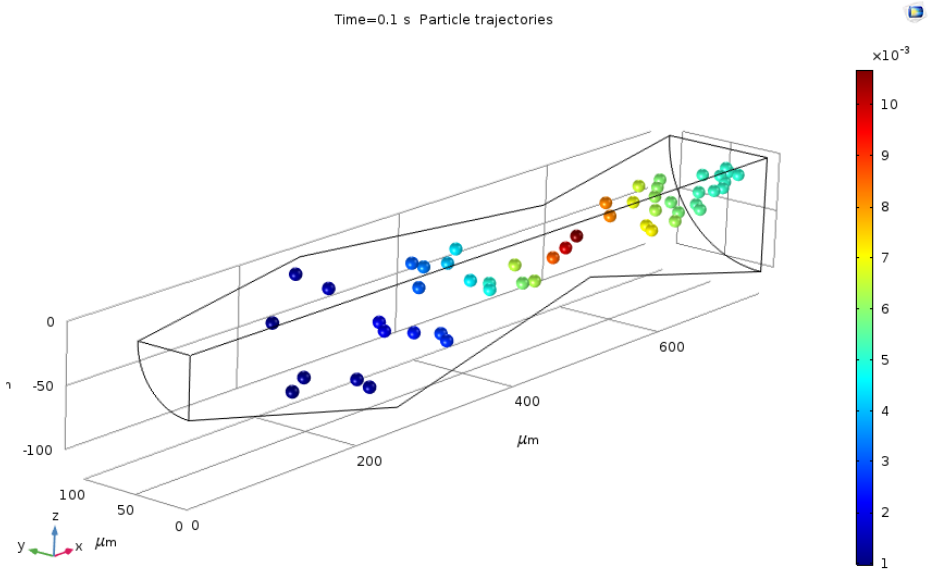

Figure 4.16: Particle trajectories inside the periodic converging-diverging tube. Color scale represents the magnitude of particle velocities.

4.2.3 Non-Equilibrium Parameter Determination

Followed the same steps with straight tube model, the NE parameters were evaluated within COMSOL. Simulation results were matched with harmonic oscillator equation to obtain the magnitude (A) and damping ratio (ζ) values. P10, P50, and P90 on cumulative distribution functions (CDF) of A and ζ were recorded separately.

The NE parameter as a function of time for 1 cp fluid viscosity case can be seen below as **Fig 4.17**. According to the figure, the particle experiences three mains stages depending on the flow path geometry. The flow geometry for the first stage is divergent shaped flow path. The NE parameter is less than zero, which means that particle velocity exceeds fluid velocity when the tube radius getting bigger. At early time, there is big difference between particle velocity and fluid velocity. At late time, particle velocity gets close to fluid velocity indicating they are close to equilibrium state. After the first stage, the flow path geometry switch to convergent shape. The NE parameter is larger than zero. It implies that particle velocity is always less than fluid velocity. In contrary to system behavior in divergent flow path, particle and fluid velocity will never getting close to each other, which indicates that the non-equilibrium will always happen. The reason for the NE parameter drops at late time is because the flow path geometry transit from converting to diverging pattern. When particle flows into another divergent flow path, which is the third stage, the behavior of particle and fluid is same with that of the first stage.

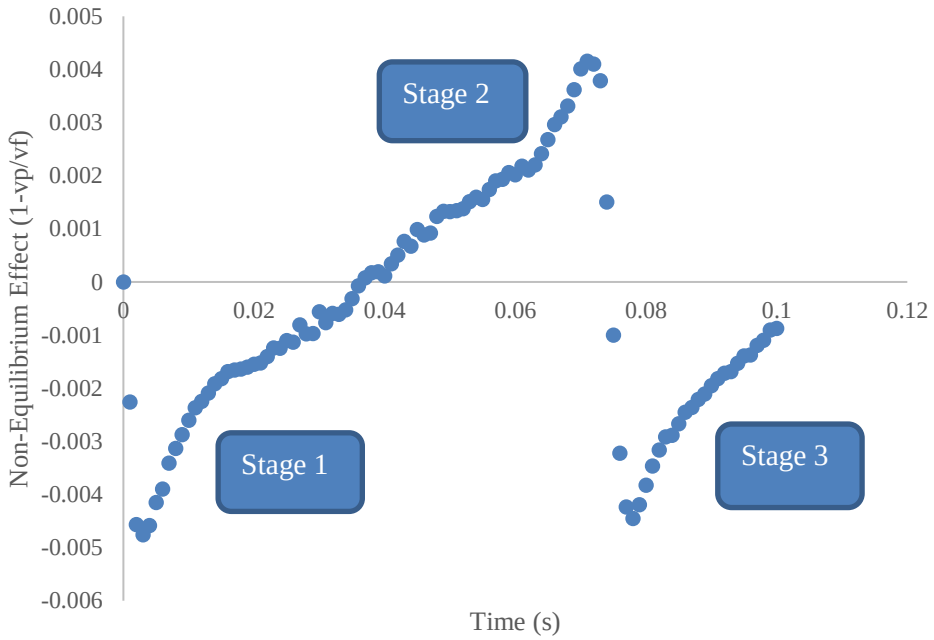

Figure 4.17: NE parameter as a function of time in periodic converging-diverging tube solved with COMSOL.

The harmonic oscillation equation was implemented to match with simulation results for different stages separately. The initial time for all three stages were normalized to zero for curve fitting. The curve fitting result for a single particle in stage 2 can be seen below as **Fig 4.18**. The A and ζ values were determined to be 2.4×10^{-5} and -0.978. In frictional vibration, negative damping causes system instability (Chen, 2014). In this situation, it indicates that the NE parameter get increased. Since particle flowed in converging tube, it can be concluded that negative ζ implies convergent flow path geometry. In analysis, the linear stability is able to predict the existence of system instability. The level of instability can be obtained through non-linear analysis, but in this

case, there is no need for analysis of its behavior since system will never achieve equilibrium.

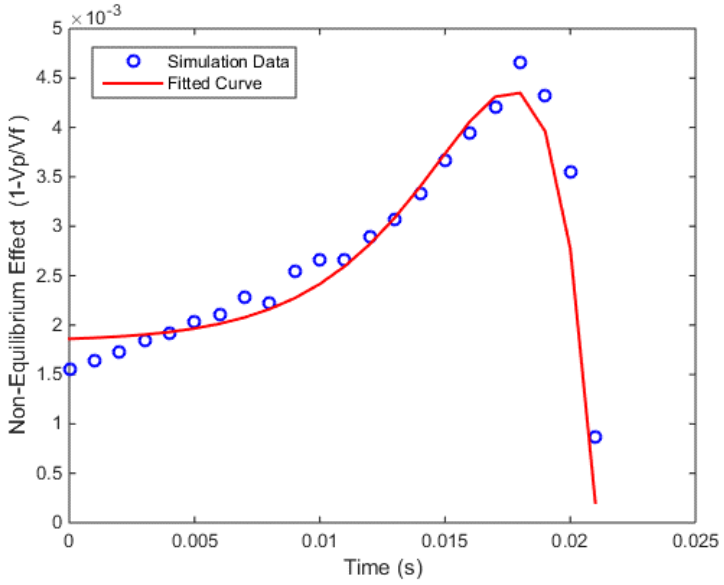

Figure 4.18: Curve fitting for single particle in stage 2 using MATLAB.

Stage 1 and stage 3 had same particle-fluid behavior, the fitting curve is shown in **Fig 4.19**. The A and ζ values were determined to be 0.026 and 0.94. In this case, ζ equals a positive number. It means that the NE parameter decreases over time. Since particle flowed in diverging flow path, it can be concluded that positive ζ value is an indication of divergent flow pattern.

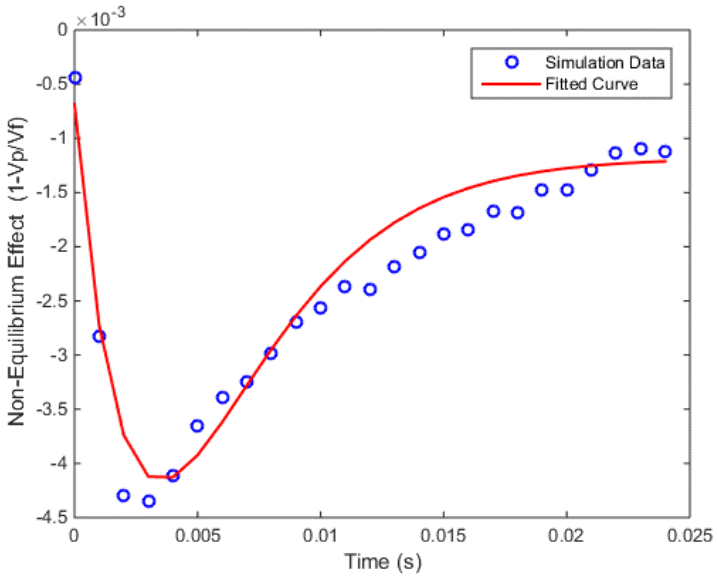

Figure 4.19: Curve fitting for single particle in stage 1 and 3 using MATLAB.

After matching all 50 particles data, the histograms and cumulative distributions function for A and ζ in divergent and convergent flow patterns were obtained separately. The statistic results for two different flow patterns are shown in **Fig 4.20** and **Fig 4.21**. In the case of $\mu = 1$ cp, the P50 values of A and ζ for convergent flow pattern are 1.9×10^{-5} and -0.894, respectively. As for divergent flow path geometry, P50 values for A and ζ are 0.015 and 0.926, respectively. The result complies with single particle case that ζ is negative when flow pattern is convergent shape, whereas ζ is positive when flow pattern is divergent shape. Moreover, the result indicates that the A value for convergent flow pattern is smaller than that of divergent flow pattern.

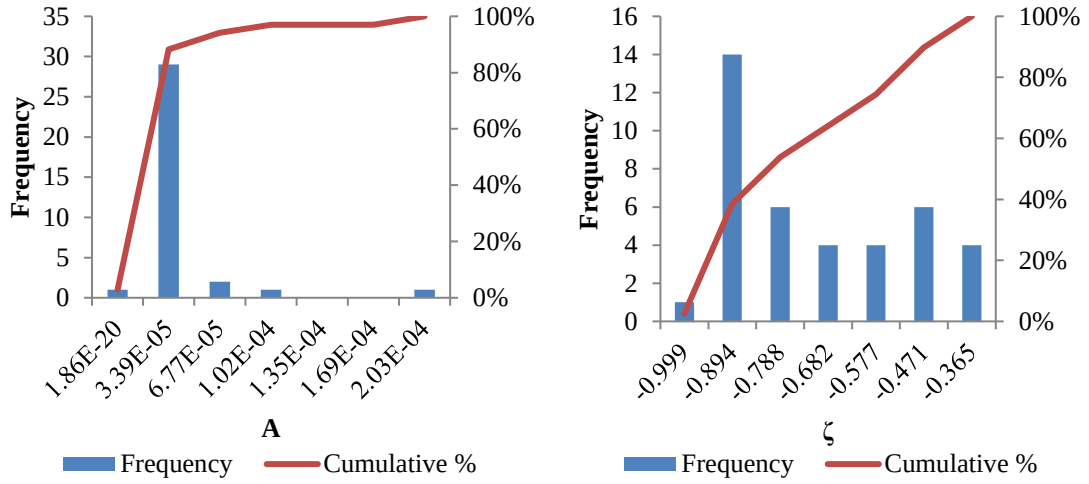

Figure 4.20: Histograms and CDFs of A and ζ values in convergent flow pattern condition for case of $\mu = 1$ cp.

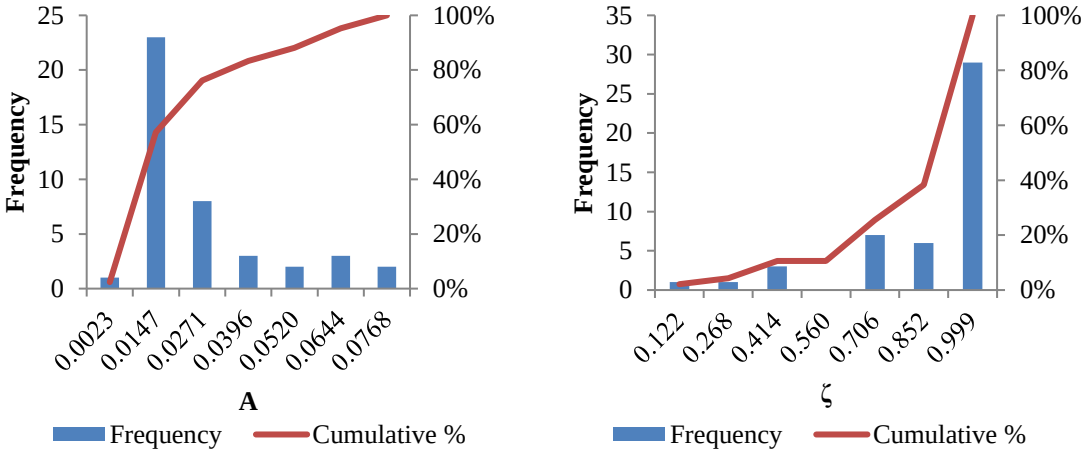

Figure 4.21: Histograms and CDFs of A and ζ values in divergent flow pattern condition for case of $\mu = 1$ cp.

4.2.5 Decouple Particle Equation from Fluid Equation

The particle transport equation is obtained by combining fluid equation with NE equation. All coefficients in harmonic oscillation equation that used to describe NE were

obtained from P50 values on their cumulative distribution functions. Coefficients for convergent flow path geometry is shown in **Table 4.4**.

Table 4.4: Coefficients in harmonic oscillation equation for converging flow pattern

Coefficient	P50	P10	P90
A	1.9×10^{-5}	2.8×10^{-6}	5.1×10^{-5}
ζ	-0.894	-0.999	-0.471
ω_0	421	182	1900
φ	100	100	100

Plug P50 values of those coefficients into **Eq 3.11**, the NE equation for convergent flow pattern yields to be

$$1-\frac{v_p}{v_f}=1.9\times10^{-5}e^{376t}\sin\left(189t+100\right) \tag{4.14}$$

Combine **Eq. 4.12** with **Eq. 4.14**, we can get the particle velocity equation for any given radius (r), axial location (z), and time (t) in convergent tube, which is

$$v_p(r,z,t)=4.5\times10^{-3}\left[\frac{1\times10^{-4}}{1\times10^{-4}-\frac{z}{5}}\right]^2\left[1-\left(\frac{r}{1\times10^{-4}-\frac{z}{5}}\right)^2\right]\left[1-1.9\times10^{-5}e^{376t}\sin\left(189t+100\right)\right] \tag{4.15}$$

$t\in[0,0.025], z\in[0,2.5\times10^{-4}]$

Coefficients for divergent flow path geometry is shown in **Table 4.5**.

Table 4.5: Coefficients in harmonic oscillation equation for diverging flow pattern

Coefficient	P50	P10	P90
A	0.015	0.008	0.058
ζ	0.926	0.268	0.999
ω_0	237	85	394
φ	100	100	100

Plug P50 values of those coefficients into **Eq 3.11**, the NE equation for divergent flow pattern is obtained to be

$$1-\frac{v_p}{v_f}=0.015e^{-220t}\sin\left(90t+100\right) \tag{4.16}$$

Combine **Eq. 4.12** with **Eq. 4.16**, the particle velocity equation for any given radius (r), axial location (z), and time (t) in convergent tube is determined to be

$$v_p(r,z,t)=0.014\left[\frac{5\times10^{-5}}{5\times10^{-5}+\frac{z}{5}}\right]^2\left[1-\left(\frac{r}{5\times10^{-5}+\frac{z}{5}}\right)^2\right]\left[1-0.015e^{-220t}\sin\left(90t+100\right)\right] \tag{4.17}$$

$t\in[0,0.025], z\in[0,2.5\times10^{-4}]$

4.2.4 Sensitivity Analysis

Sensitivity analysis was performed on fluid viscosity to investigate how viscosity affect NE parameters. Simulations were set for another two cases, which are $\mu = 4$cp and 0.5 cp. The histograms and cumulative distribution functions for two cases are presented in **Figs 4.22-4.23.**

In the case of $\mu = 4$ cp, the P50 values of A and ζ for convergent flow pattern were determined to be 6.1×10^{-6} and -0.911, respectively. For divergent flow pattern, the P50 values of A and ζ values were determined to be 2.43×10^{-3} and 0.999, respectively.

In the case of $\mu = 0.5$ cp, the P50 values for A and ζ for convergent flow pattern were determined to be $1.42\times10^{-3}$and 0.724, respectively. For divergent flow pattern, the P50 values of A and ζ values were determined to be 0.69 and 0.741, respectively.

Both cases have consistent results with the case of $\mu = 1$ cp that ζ value is negative in convergent flow path geometry, whereas ζ value is positive for divergent flow pattern.

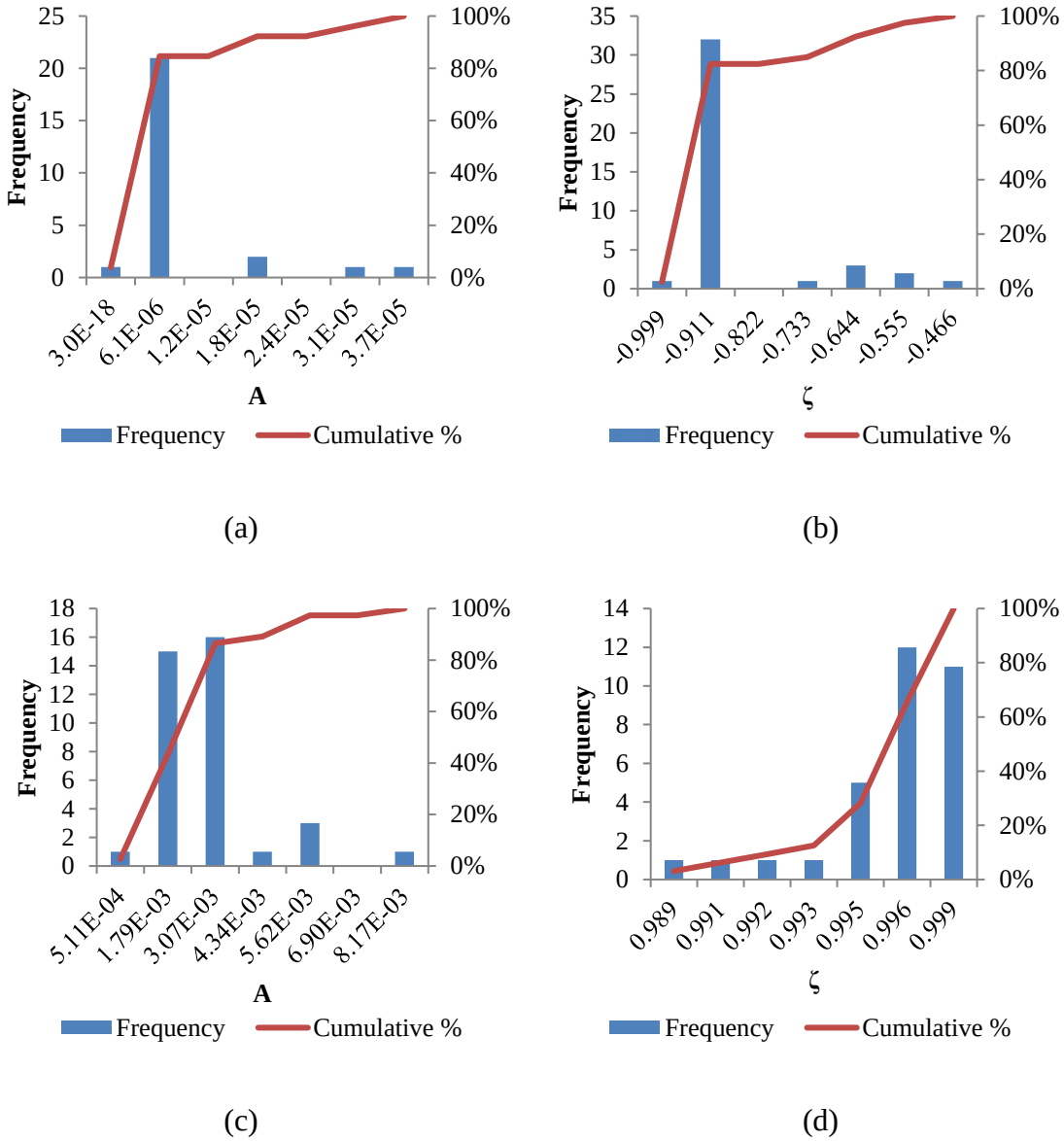

Figure 4.22: Statistic results for the case of 4 cp. (a) and (b) are the histograms and CDFs of A and ζ for convergent flow pattern. (c) and (d) are the histograms and CDFs of A and ζ for divergent flow pattern.

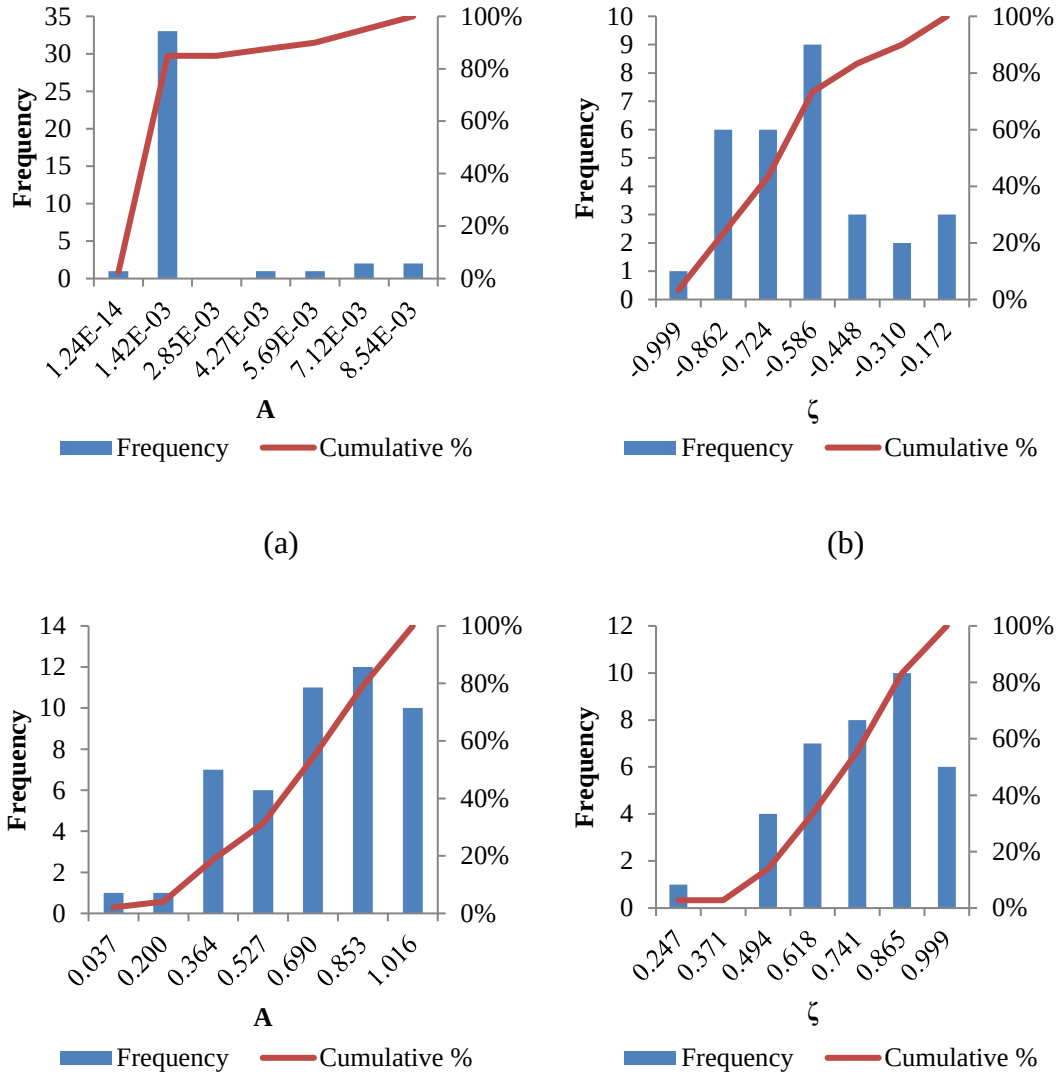

Figure 4.23: Statistic results for the case of 0.5 cp. (a) and (b) are the histograms and CDFs of A and ζ for convergent flow pattern. (c) and (d) are the histograms and CDFs of A and ζ for divergent flow pattern.

The A and ζ values for different flow patterns are plotted separately. Since in convergent flow path geometry, particle and fluid can never achieve equilibrium state, there is no need for the investigation of the relationship between ζ value and fluid

viscosity under this situation. The comparison results can be seen below as **Fig 4.24**. In terms of NE oscillation amplitude, high viscosity fluid has low value of A for both convergent and divergent flow patterns indicating there are small magnitudes of NE effect between particle and fluid in high viscosity fluid. As for damping ratio, reducing fluid viscosity leads to a decreased value of ζ. It implies that in high viscosity fluid, it takes shorter time for particle to attain equilibrium with its carrier fluid in divergent flow pattern.

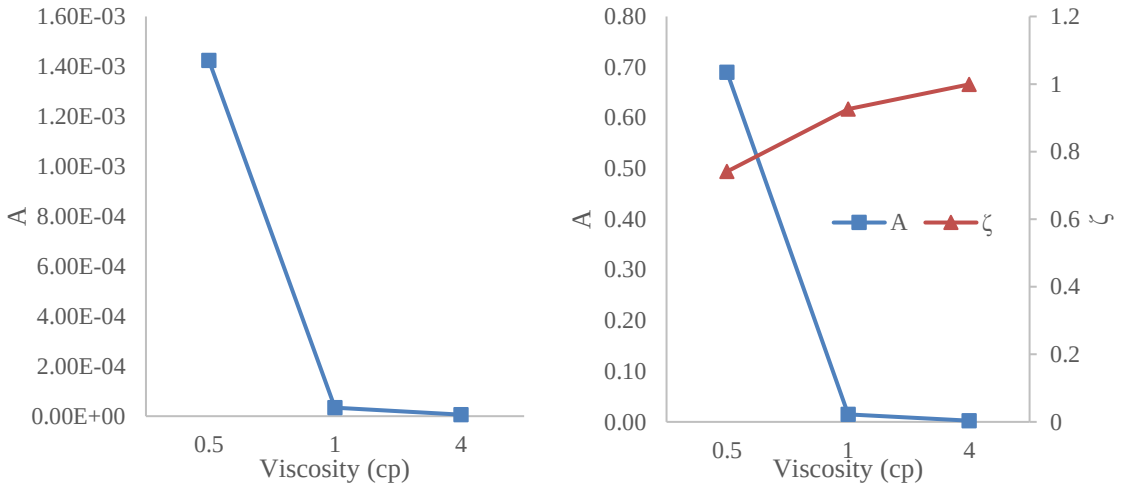

(a) (b)

Figure 4.24: Relationship between NE parameter with fluid viscosity. (a) demonstrates the relationship between A value and fluid viscosity in convergent flow pattern. (b) represents the trends of A and ζ changing with fluid viscosity.

Chapter 5: Non-Equilibrium Effect in Actual Pore Network

5.1 Scanning Electron Microscope Image of Pore Network

5.1.1 Extract Geometry Pattern from Rock Sample

In this chapter, the Non-Equilibrium effect study is performed using actual pore network. Sirivithayapakorn and Keller (2003) created some scanning electron microscope (SEM) images of thinly sliced rock samples by etching the geometry patterns to silicon wafers. It can be seen in **Fig 5.1**.

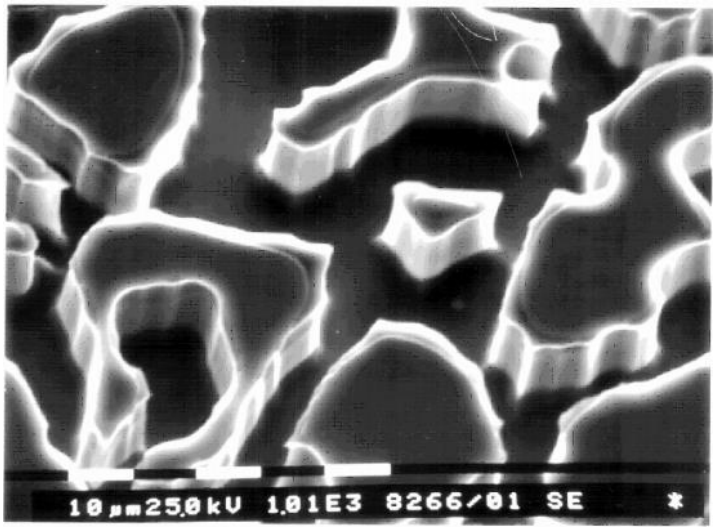

Figure 5.1: SEM image of the geometry patterns in the silicon wafer.

Using image processing technique, the SEM image was digitized and transferred to binary image, which can be seen below as **Fig 5.2**. The size of the image is 640 μm by 320 μm. The black region represents the pore space. The white region represents the rock grain.

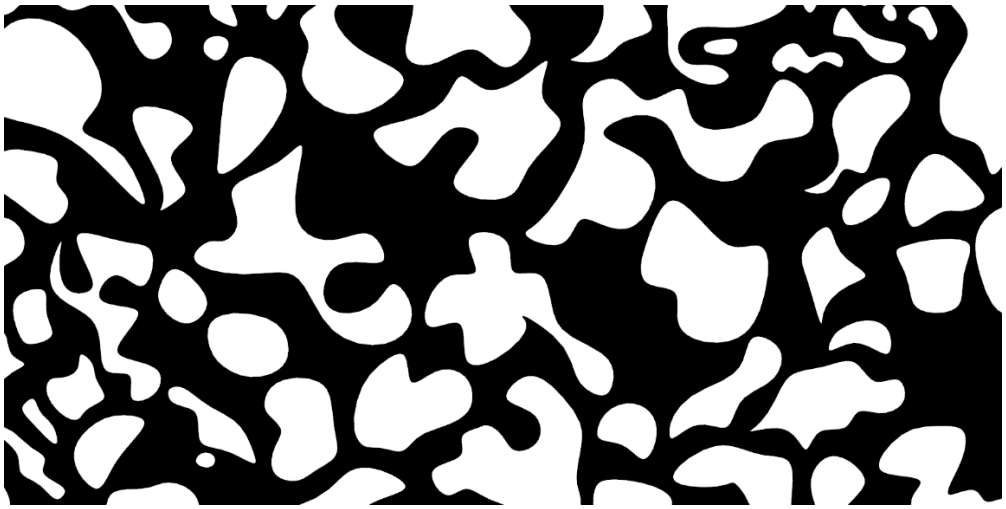

Figure 5.2: Binary image of the SEM pore structure.

5.1.2 Porosity and Pore Size Distribution from SEM Image

The pore area is evaluated by using surface integration over the pore space within COMSOL. The total pore area and porosity are determined to be 109547.5 μm^2 and 0.553.

The pore size distribution is determined by using MATLAB code designed by Rabbani et al (2014). It is based on watershed segmentation algorithm, which can detect and separate pores by cutting the image on the watershed ridge line. The cut structure is illustrated in **Fig 5.3**.

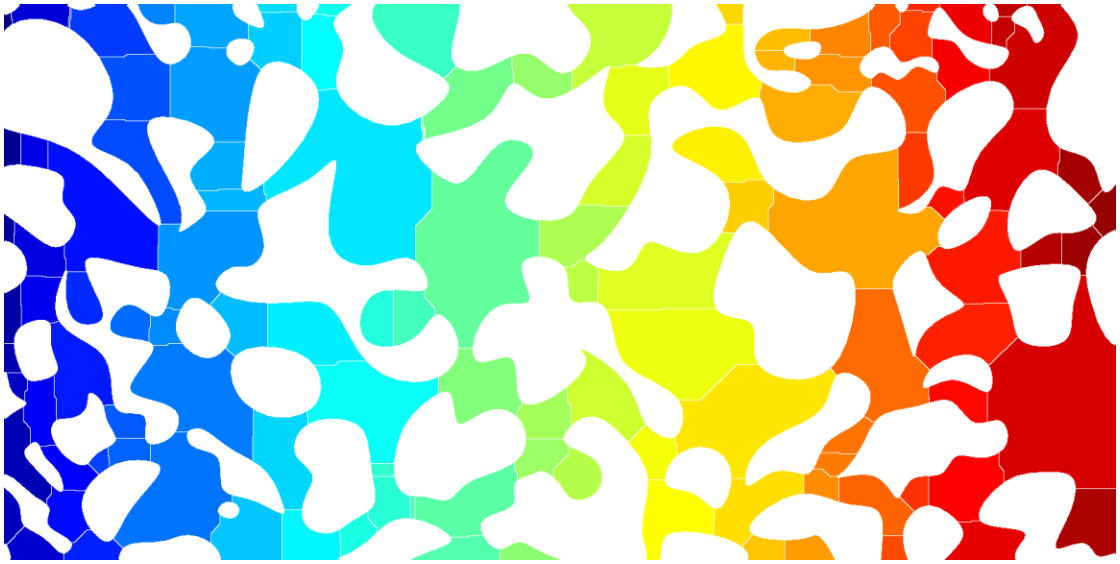

Figure 5.3: Separation of pores base on watershed segmentation algorithm. The white lines are watershed ridge lines

Assuming that each segment is circle shape, the pore radius can be determined. The pore size distribution is shown below as **Fig 5.4**. The average pore radius is 15 μm.

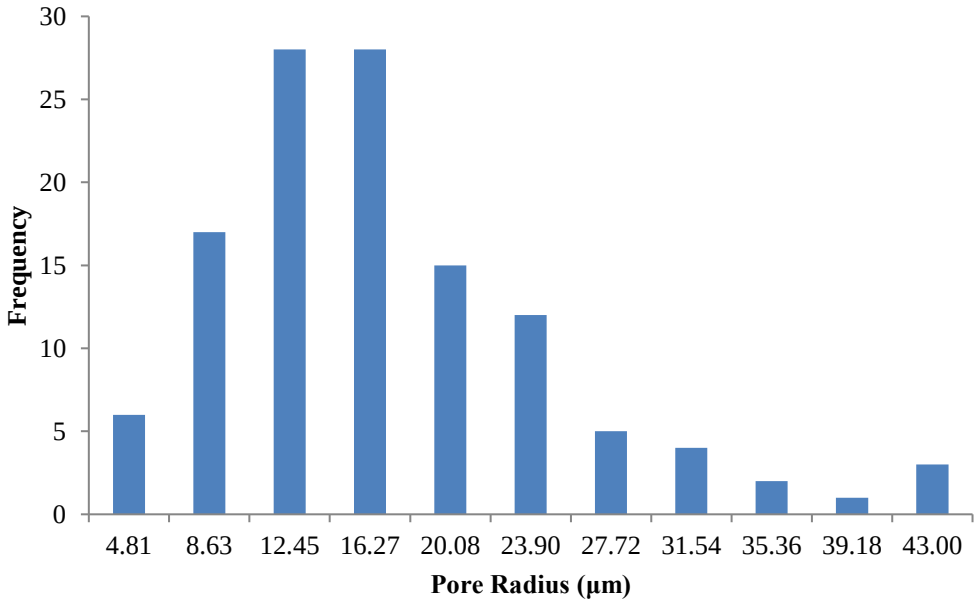

Figure 5.4: The pore size distribution of the SEM pore structure.

5.2 Model set up

The first step of the research is to investigate the single particle transport behavior in porous media. The SEM image was transferred to DXF file, which can be imported into COMSOL. The imported image is shown in **Fig 5.5**. The laminar flow interface in COMSOL was implemented to solve fluid flow equation, and particle tracing interface was used to calculate particle motion. Single particle was injected from the inlet to outlet boundary in the same velocity as fluid velocity. The particle and fluid properties are listed in **Table 5.1**.

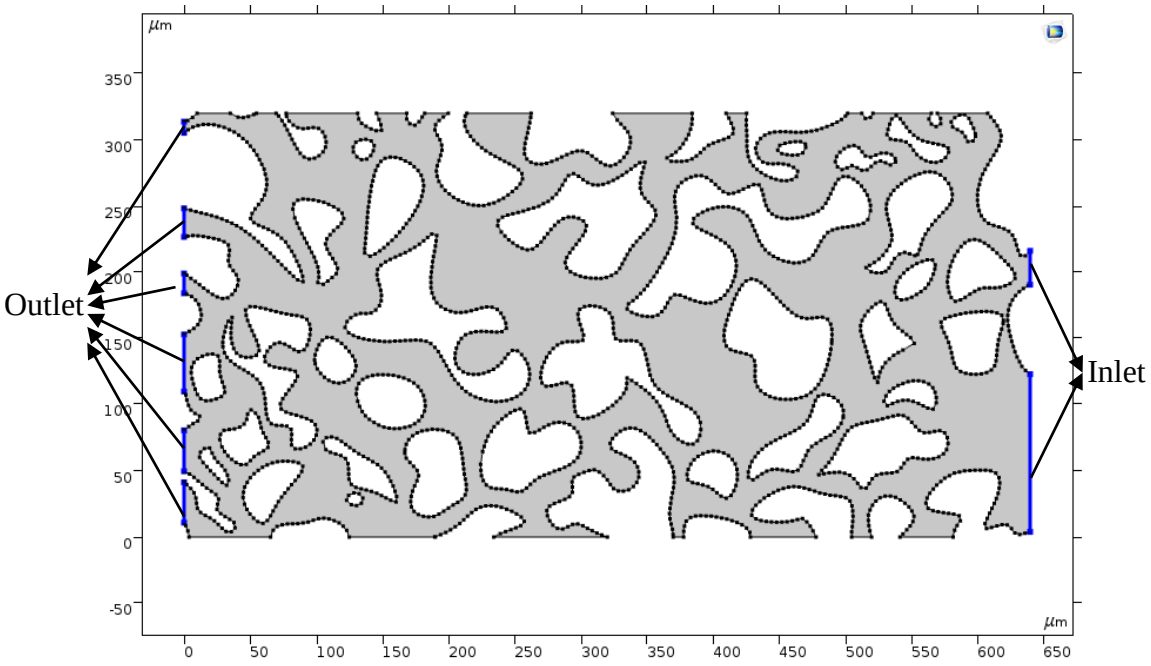

Figure 5.5: SEM image of pore structure in COMSOL format.

Table 5.1: Simulation inputs for SEM pore structure.

Parameter	Value	Unit
Fluid Density	750	kg/m^3
Fluid Viscosity	1	cp
Initial Velocity	0.004	m/s
Particle Diameter	10	μm
Particle Density	2000	kg/m^3

5.3 Fluid Velocity Profile and Particle Trajectory

The fluid velocity distribution inside the pore structure is demonstrated in **Fig 5.5**. The velocity profile follows Poiseuille's law that high velocity occurs at small pore throats, and low velocity occurs at big pore channels.

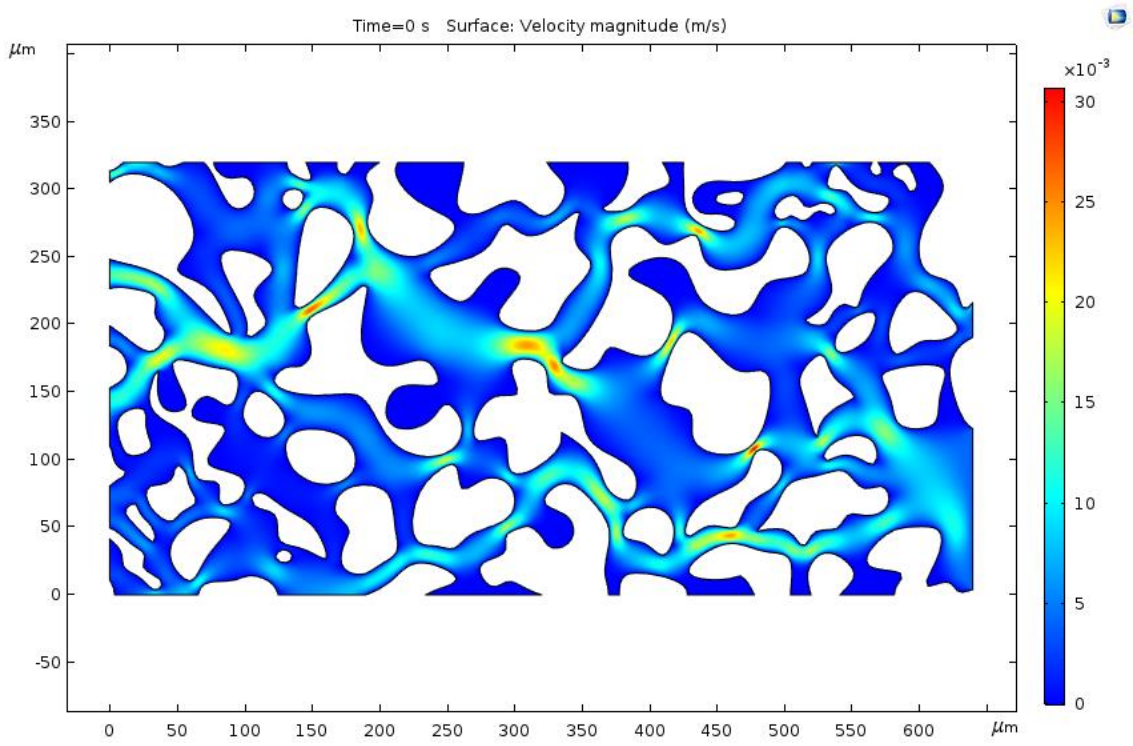

Figure 5.6: Fluid velocity field in the pore network solved with CFD module in COMSOL.

The single particle trajectory is shown below as **Fig 5.7**. With only the effect of drag force generated by fluid flow field, particle moving behavior is similar to fluid flowing behavior, which manifest that particle moves faster in tiny pores, and moves slower in big pores.

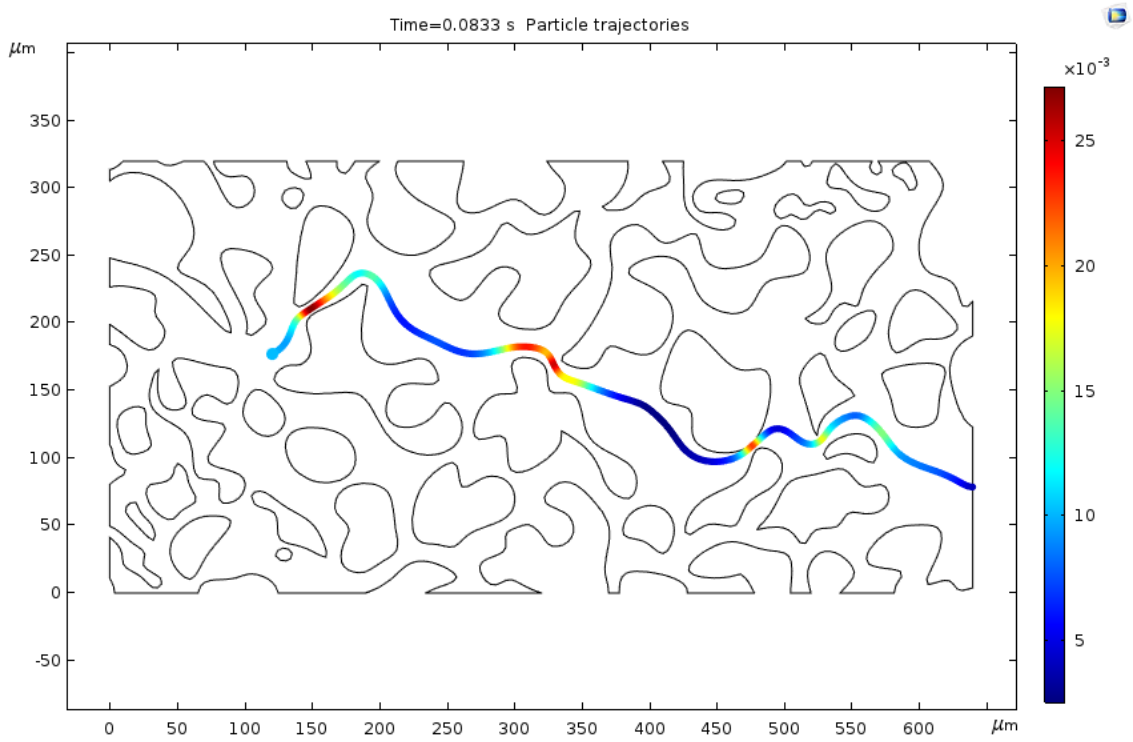

Figure 5.7: The simulated particle trajectory inside the pore network. The rainbow color represents the magnitude of particle velocity.

5.4 Non-Equilibrium Parameter Determination

The NE effect for single particle was evaluated in COMSOL. The NE as a function of time for single particle injection is plotted in **Fig 5.8**. Due to the complexity of the pore structure, the trends of NE variation over time are not identical. As discussed in chapter 4, NE larger than zero indicates particles move through converging flow pattern, whereas NE less than zero implies particles move in diverging flow pattern. In

addition, different shaped pores are supposed to have different oscillation behaviors, which manifest as distinct curve shapes in the figure. Therefore, based on the flow pattern criteria and the shape of NE curve, the NE curve can be divided into several stages. For example, from t=0 to t=0.01s, the NE is above zero, which is an indication of converging flow path geometry. Meanwhile, there are two distinct curve shapes, which means that particle moves in two different pores.

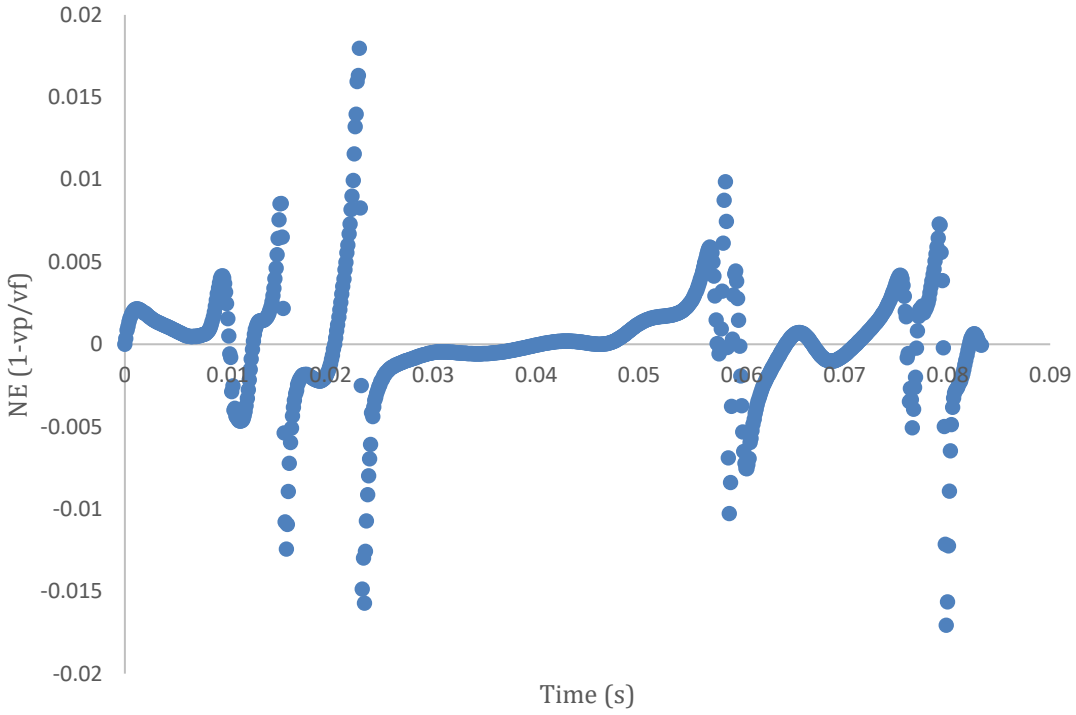

Figure 5.8: NE as a function of time for single particle injection.

After detecting the flow path and the curve shape, 20 stages were identified. In order to investigate particle transport behavior, the harmonic oscillation equation was implemented to match the data for each stage. The initial time for each stage was normalized to zero for curve fitting. The oscillator amplitudes and damping ratios were

obtained and demonstrated in **Table 5.2**. The results present that in converging flow pattern, ζ values are less than zero, which consists with the results obtained in chapter 4. It means that particle velocity is always less than fluid velocity, and they can never achieve equilibrium with each other. In diverging flow pattern, the result shows that ζ values are greater than zero. It also consists with previous observation. As discussed previously, particle velocity is greater than fluid velocity in diverging flow path. In addition, by comparing A and ζ values with the pore geometry for each stage, it was observed that the more divergent the pore shape is, the higher A and ζ values will be obtained. It means that highly divergent flow pattern has large magnitude of NE, but it takes short time for particle and fluid to attain equilibrium state.

Table 5.2: A and ζ values for 20 stages obtained from curve fitting. The flow pattern for each stage is indicated.

Stages	A	ζ	Flow Pattern
1	0.05851	0.996	divergent
2	0.00048	-0.779	convergent
3	0.00586	0.124	divergent
4	0.00014	-0.967	convergent
5	0.24265	0.996	divergent
6	0.00225	0.122	divergent
7	0.00052	-0.975	convergent
8	0.01425	0.922	divergent
9	0.00123	-0.286	convergent
10	0.00015	-0.941	convergent
11	0.00100	-0.616	convergent
12	0.01388	0.223	divergent
13	0.00214	-0.287	convergent
14	0.03774	0.944	divergent
15	0.00070	-0.013	convergent
16	0.00143	0.221	divergent
17	0.00017	-0.953	convergent
18	0.00408	0.024	divergent
19	0.00107	-0.975	convergent
20	0.12454	0.955	divergent

Using all coefficients (A, ζ, ω_0, φ) gotten from the curve fitting, the matched NE curve for all stages can be obtained and they can be seen below as **Fig 5.9**. The fitted curve has good match with the original NE curve that evaluated in simulation.

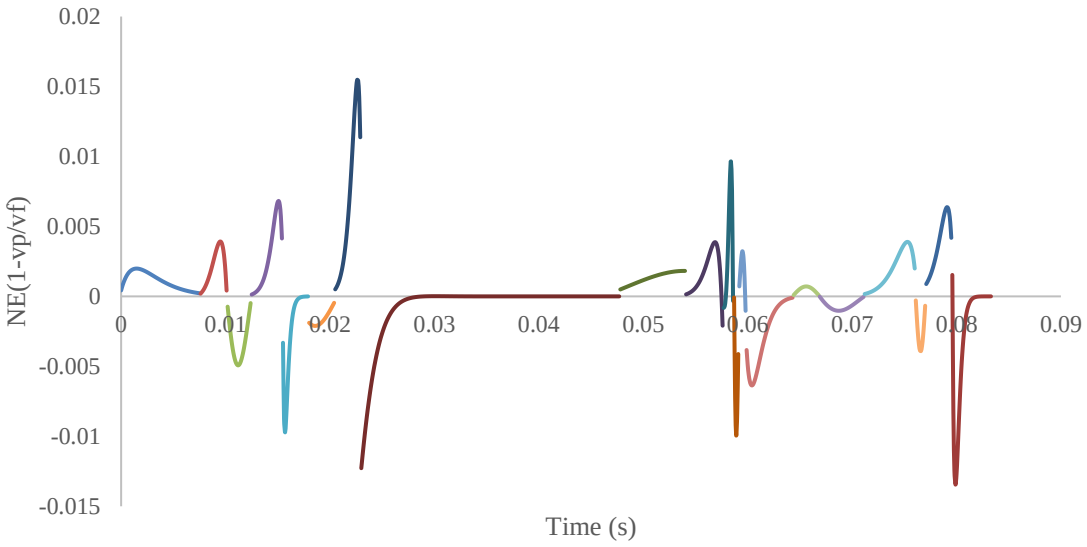

Figure 5.9: NE curve obtained by curve fitting. Each color represents one stage.

5.4 Equivalent Tube Radius determination for Pore Structure

5.4.1 Multiple-Particle Injection

In order to have a better characterization of particle transport behavior in porous media, the motions of multiple particles in different size of pores need to be investigated. Simulations were performed for different numbers of particle injections. The simulation details are listed in **Table 5.3**. Particles were injected from the inlet boundary to outlet boundary. Simulations were stopped after most particles breakthrough from the outlet boundary. Fluid was injected for approximately 3 PV (pore volume).

Table 5.3: Simulation inputs for multiple particles injection

Parameter	Value	Unit
Fluid density	750	kg/m^3
Fluid viscosity	1	cp
Initial velocity	0.004	m/s
Particle diameter	0.5	μm
Particle density	2000	kg/m^3
Number of particles	5-20	-

The first simulation was performed on 5 particles injection. The particle trajectories are demonstrated in **Fig 5.10**. Comparing with the fluid velocity distribution inside the pore network (**Fig 5.6**), particles tend to move in high velocity region with the effect of drag force.

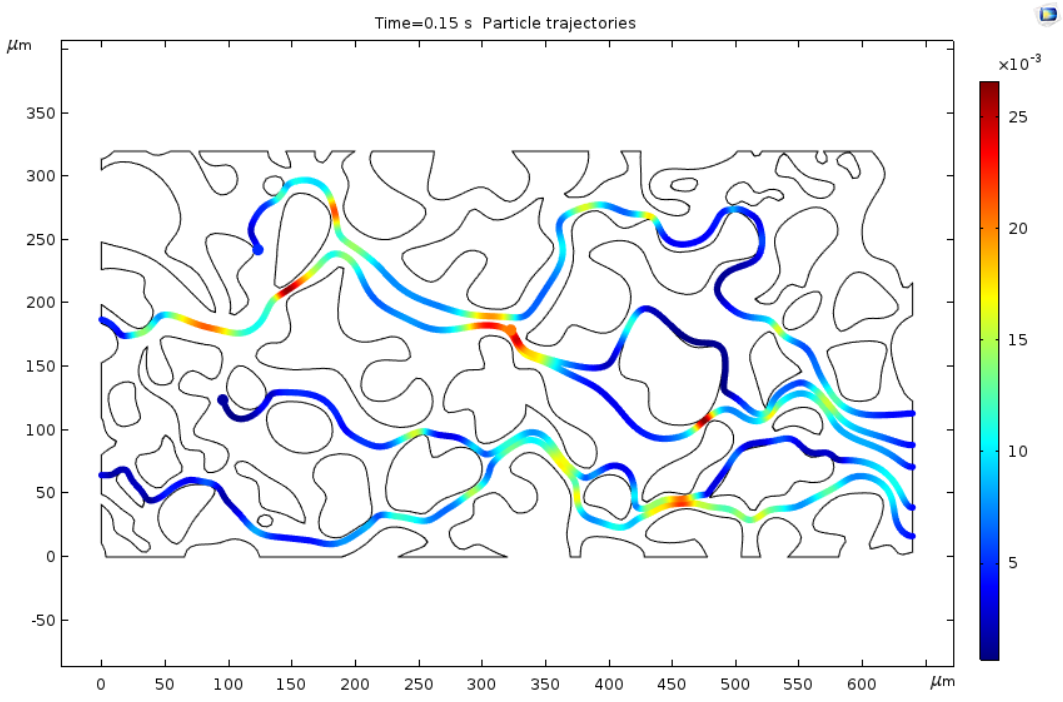

Figure 5.10: Particle trajectories for 5 particles injection. The color scale represents the magnitude of particle velocity.

After the simulation results were obtained, MATLAB code was designed to identify different stages in which particles move through different size of pores, and then use harmonic oscillation equation to match with results for all stages to obtain the A values. The histograms of A values for convergent and divergent flow patterns can be seen in **Fig 5.11**.

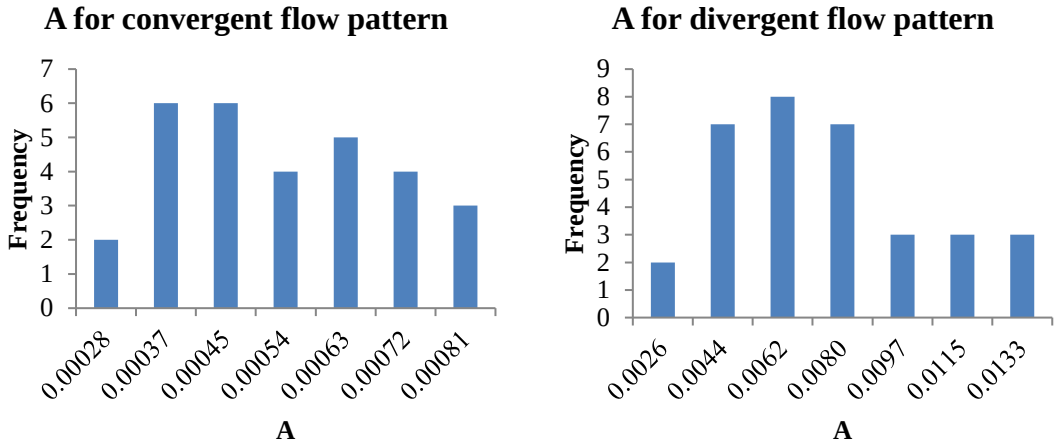

Figure 5.11: Histograms of A value for convergent and divergent flow patterns in the case of 5 particles injection.

5.4.2 Estimate the Equivalent Tube Radius for Each Stage

Purcell proposed the first theoretical pore-network model called the bundle-of-tube model to characterize the porous media of sandstone formations (Zheng. 2018). This model determines series of parallel circular tubes with different radii based on mercury drainage experiments.

The rationale for defining an equivalent radius is that since each stage has its corresponding A value in the multiple particles injection simulation, *it is hypothesized that there is an equivalent tube radius that can give the same A value for each stage*. In

order to determine the equivalent pore radii for all stages, another converging-diverging model simulation, which has been discussed in chapter 4 was performed. According to the pore size distribution of the pore structure, the minimum and maximum pore radii are 4.81 μm and 43 μm, respectively. The converging-diverging models were set up with a fixed minimum tube radius of 5 μm, and variable maximum tube radius ranging from 10 μm to 45 μm. The length of each tube was set to be 50 μm. The schematic model is demonstrated in **Fig 5.12**.

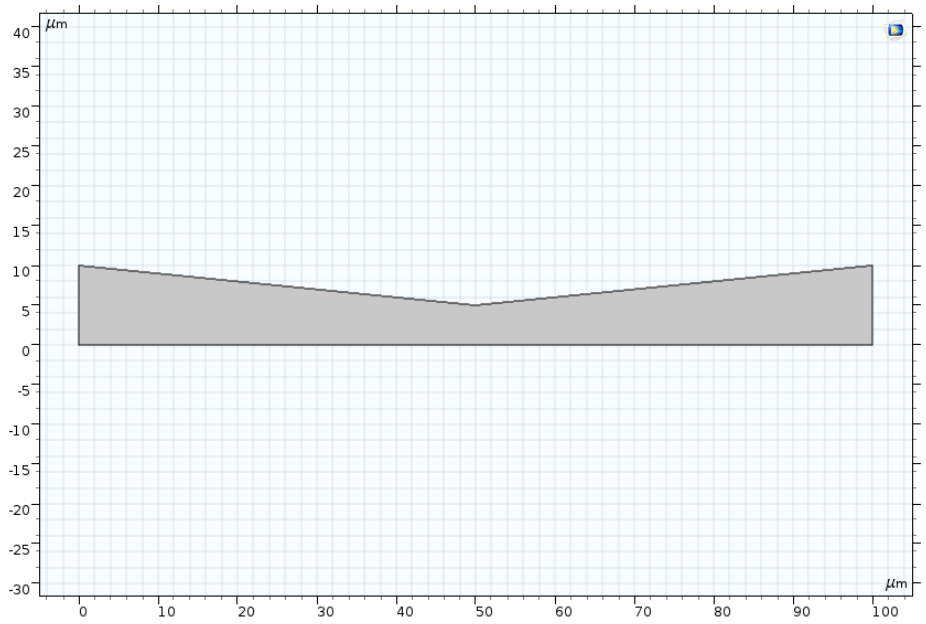

Figure 5.12: Schematic cross-section of converging-diverging tube.

Harmonic oscillation equation was applied to match with simulation results for convergent and divergent flow pattern separately to obtain A values in different flow patterns. The relationships between maximum radius and A value for convergent and divergent flow patterns are shown in **Fig 5.13**. The results indicate that there are

approximately linear relationships between tube radius and A value for different flow patterns.

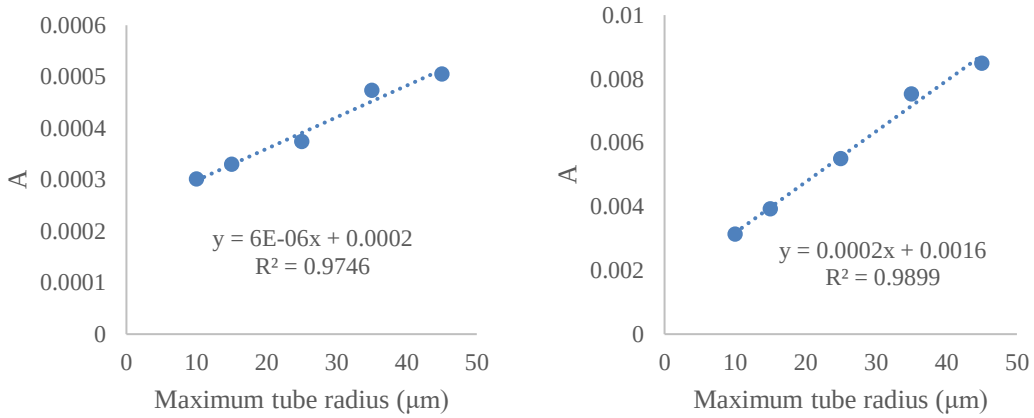

(a) (b)

Figure 5.13: Corresponding A values for different maximum radius in (a) convergent flow pattern, and (b) divergent flow pattern.

Using the trend line equations, the maximum radius for each A value can be determined. The average value of maximum and minimum tube radii was approximated to be the equivalent tubr radius of the corresponding stage. For convergent flow pattern, the equivalent tube radius (r_e) is estimated to be

$$r_e = \frac{R_{\max} + R_{\min}}{2} = 79375.5A - 16 \tag{5.1}$$

For divergent flow pattern, the equivalent tube radius (r_e) is estimated to be

$$r_e = \frac{R_{\max} + R_{\min}}{2} = 3116.7A - 2.3 \tag{5.2}$$

The estimated pore radius distribution for paths that 5 particles move through is shown in **Fig 5.14**. Similar to the pore size distribution of the rock sample, most radii are between 16-28 μm.

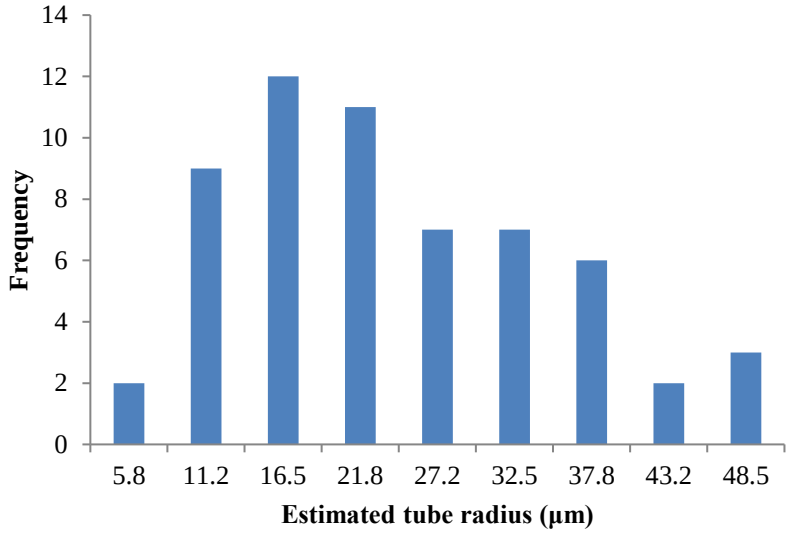

Figure 5.14: Histogram for estimated tube radius for 5 particles injection.

Same simulations were performed for particle number of 10, 15, and 20. The particle trajectories and estimated tube radius distribution result can be seen below as **Figs 5.15-5.17**. Same as discovered in 5 particles injection case, particles tend to move to high fluid velocity region. There are some pore spaces that particles can never reach with only the effect of drag force. Moreover, it was observed that some particles share same paths inside the pore structure. The more particles are being injected, the more repeated flow paths are observed. Therefore, some tube radii were calculated more than once, and that is the reason why the number of estimated pore radius for identical pore throat increase when more particles are injected. Consequently, in order to have better

characterization of the pore space that particle move through, there is no need to inject too many particles because they may have repeated paths, which yields over-estimation of equivalent pores number. Among those results, 5 particles injection provides better characterization of the pore network, and the equivalent tube radius distribution (**Fig. 5.14**) can be used to represent pore spaces that particle move through in this pore network.

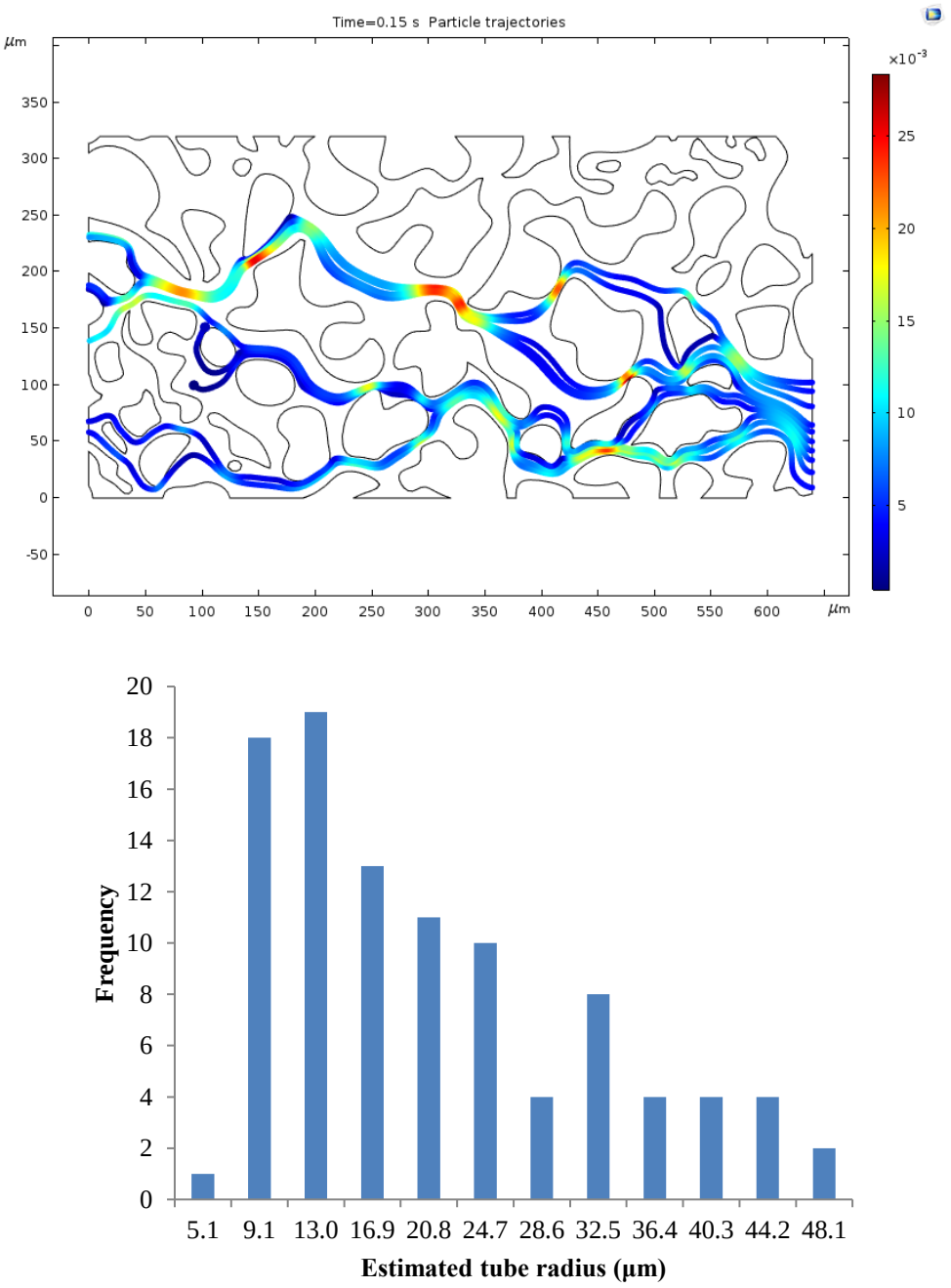

Figure 5.15: Particle trajectories (top) and histogram of estimated tube radius (bottom) for 10 particles injection.

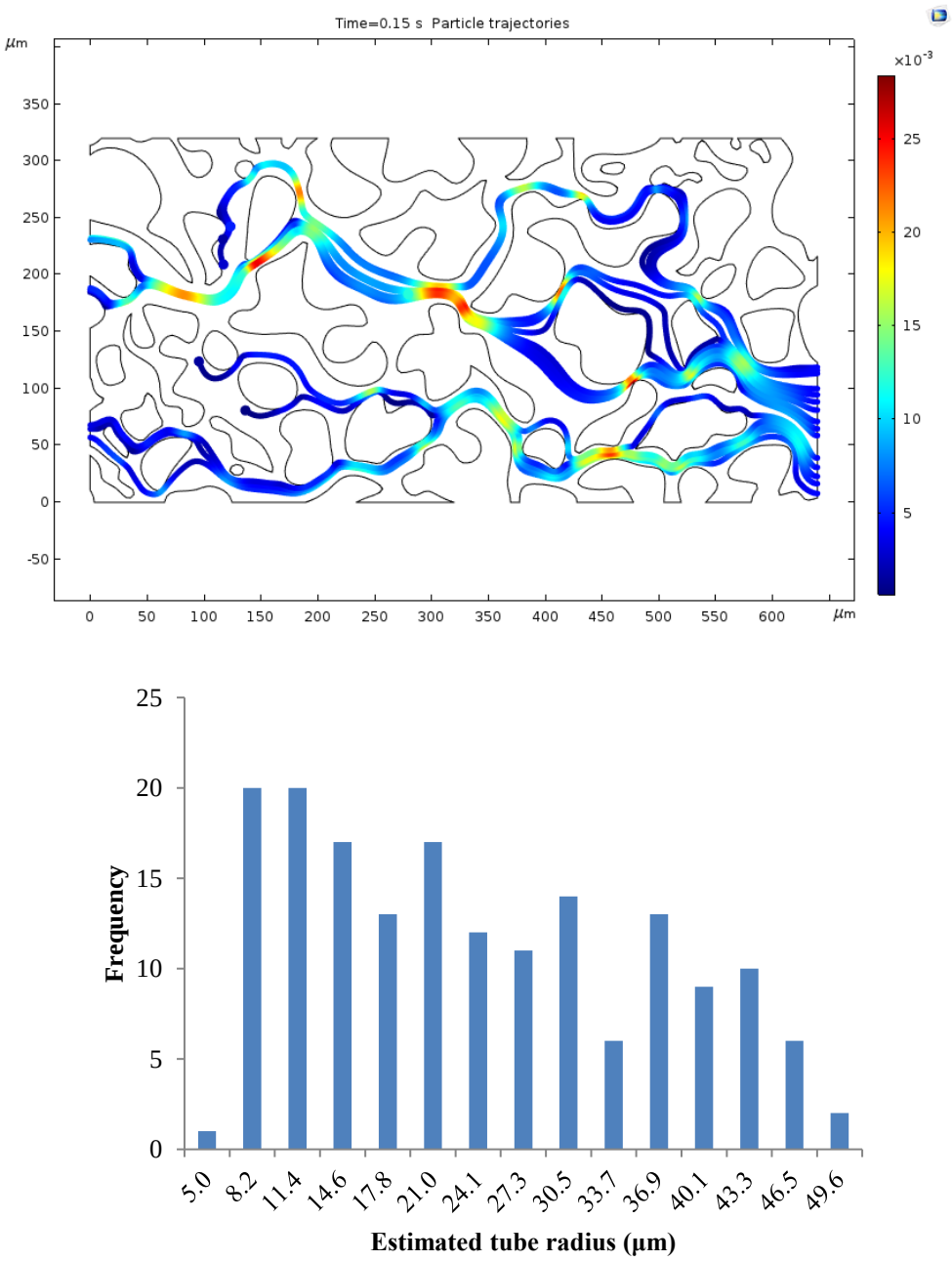

Figure 5.16: Particle trajectories (top) and histogram of estimated tube radius (bottom) for 15 particles injection.

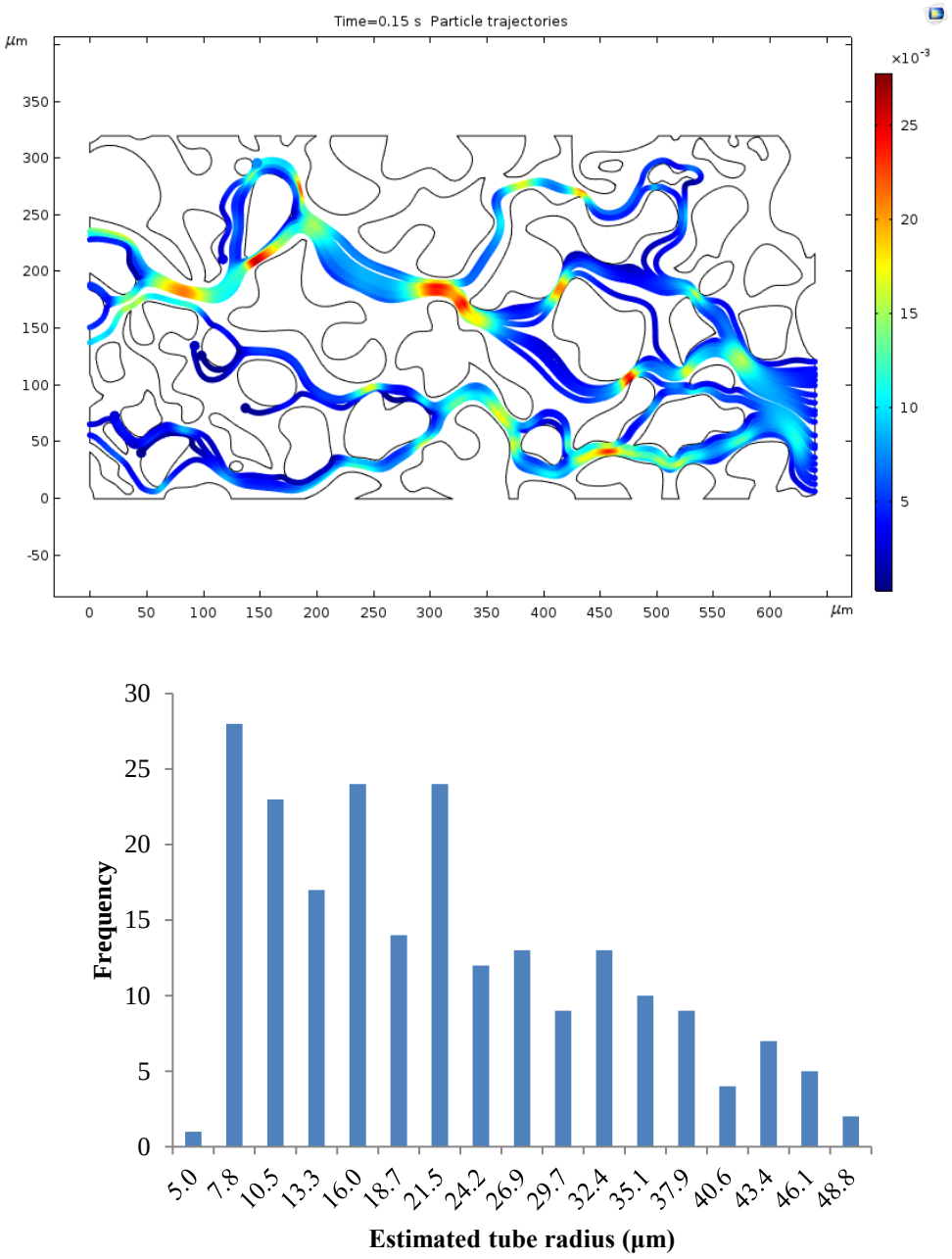

Figure 5.17: Particle trajectories (top) and histogram of estimated tube radius (bottom) for 20 particles injection.

Chapter 6: Conclusions and Recommended Future Work

6.1 Conclusions

In this thesis, the NE effect in particulate flow system was investigated by developing particle transport models in straight tube, periodic converging-diverging shaped tube, and actual pore structure. Adapted harmonic oscillation equation was implemented to describe the NE effect between particle and carrier fluid. The thesis was hypothesizing whether the linear theory of stability can explain non-equilibrium evolution in particulate systems through general form of harmonic oscillation equation. The determination of oscillation parameters was achieved by using curve fitting in MATLAB. The influence of fluid viscosity, tube radius, and flow path geometry on the NE effect were addressed. The main conclusions are drawn as follows:

1. The time variation of the NE effect complies with the theory of stability. Harmonic oscillation equation can be used to characterize the NE effect in particulate flow system.
2. Two key parameters of oscillator equation are amplitude (A) and damping ratio (ζ). The former represents the magnitude of NE and the latter is an indication of flow path geometry as well as time needed to attain equilibrium.
3. In divergent flow path geometry, ζ value is between 0 and 1. Reducing the fluid viscosity leads to a reduced ζ value indicating that it will take longer for particle to reach to equilibrium state. Reducing fluid viscosity yields an increased value of A indicating a larger magnitude of NE effect.

4. In convergent flow path geometry, ζ value is between 0 and -1. The NE effect increases as a function of time implying that particle velocity always remains less than the fluid velocity; hence, the system will never achieve an equilibrium state. In this situation, non-linear analysis should be used.
5. The flow simulations of SEM image present consistent results with diverging and converging flow results. The equivalent tube radii of complex pore geometries where particles move through are obtained. Particles without repeated moving paths have better assistance on the determination of equivalent pore radii using NE study.

The outcome of this work can shed light upon explaining the complex NE effects in porous media. The generalized equation to model NE can help temporarily decouple particle transport equation from fluid equations facilitating much advanced particulate flow modeling in the large-scale problems.

6.2 Recommended Future Work

In order to have an integrated understanding of the NE effects in particulate flow system, several other works can be addressed in the future:

1. Particle-particle and particle-wall interactions can be investigated.
2. Forces other than drag force, for example, gravity, lifting, buoyancy, Brownian, and electrostatic forces can be taken into considerations.
3. The study can be repeated when several fluids are present.

Reference

Auset, M., & Keller, A. A. (2004). Pore-scale processes that control dispersion of colloids in saturated porous media. Water Resources Research, 40(3).

Bahrami, M., Akbari, M., & Sinton, D. (2008, January). Laminar fully developed flow in periodically converging-diverging microtubes. In ASME 2008 6th International Conference on Nanochannels, Microchannels, and Minichannels (pp. 181-188). American Society of Mechanical Engineers.

Bedrikovetsky, P., Siqueira, F. D., Furtado, C. A., & Souza, A. L. S. (2011). Modified particle detachment model for colloidal transport in porous media. Transport in porous media, 86(2), 353-383.

Bottero, S., Hassanizadeh, S. M., Kleingeld, P. J., & Heimovaara, T. J. (2011). Nonequilibrium capillarity effects in two-phase flow through porous media at different scales. Water Resources Research, 47(10).

Chen, G. S. (2014). Handbook of friction-vibration interactions. Elsevier.

Davudov, D., Moghanloo, R. G., & Flom, J. (2018). Scaling Analysis and Its Implication for Asphaltene Deposition in a Wellbore. SPE Journal, 23(02), 274-285.

Fan, M., McClure, J., Han, Y., Li, Z., & Chen, C. (2018). Interaction Between Proppant Compaction and Single-/Multiphase Flows in a Hydraulic Fracture. SPE Journal.

Haaland, A. M. (2016). Numerical Simulation and Experimental Study of Reelwell's Heavy over Light Solution in Vertical Well Sections (Master's thesis, University of Stavanger, Norway).

Hassan, H. K., & Stepanyants, Y. A. (2017). Resonance properties of forced oscillations of particles and gaseous bubbles in a viscous fluid at small Reynolds numbers. Physics of Fluids, 29(10), 101703.

Ho-Le, K. (1988). Finite element mesh generation methods: a review and classification. Computer-aided design, 20(1), 27-38.

Hu, Z., Azmi, S. M., Raza, G., Glover, P. W., & Wen, D. (2016). Nanoparticle-assisted water-flooding in Berea sandstones. Energy & Fuels, 30(4), 2791-2804.

Kong, X., McAndrew, J., & Cisternas, P. (2016, November). CFD study of using foam fracturing fluid for proppant transport in hydraulic fractures. In Abu Dhabi International Petroleum Exhibition & Conference. Society of Petroleum Engineers.

Lake, L. W. (2006). Petroleum engineering handbook.

Marquez, M., Williams, W., Knobles, M. M., Bedrikovetsky, P., & You, Z. (2014). Fines migration in fractured wells: integrating modeling with field and laboratory data. SPE Production & Operations, 29(04), 309-322.

Multiphysics, C. O. M. S. O. L. (2018). Comsol multiphysics user guide (version 5.4 a). COMSOL.

Oliveira, M. A., Vaz, A. S., Siqueira, F. D., Yang, Y., You, Z., & Bedrikovetsky, P. (2014). Slow migration of mobilised fines during flow in reservoir rocks: laboratory study. Journal of petroleum science and engineering, 122, 534-541.

Rabbani, A., Jamshidi, S., & Salehi, S. (2014). An automated simple algorithm for realistic pore network extraction from micro-tomography images. Journal of Petroleum Science and Engineering, 123, 164-171.

Roy, P., Du Frane, W. L., & Walsh, S. D. (2015, November). Proppant transport at the fracture scale: simulation and experiment. In 49th US Rock Mechanics/Geomechanics Symposium. American Rock Mechanics Association.

Russell, T., Chequer, L., Borazjani, S., You, Z., Zeinijahromi, A., & Bedrikovetsky, P. (2018). Formation Damage by Fines Migration: Mathematical and Laboratory Modeling, Field Cases. In Formation Damage During Improved Oil Recovery(pp. 69-175).

Schwarzkopf, J. D., Sommerfeld, M., Crowe, C. T., & Tsuji, Y. (2011). Multiphase flows with droplets and particles. CRC press.

Sirivithayapakorn, S., & Keller, A. (2003). Transport of colloids in saturated porous media: A pore-scale observation of the size exclusion effect and colloid acceleration. Water Resources Research, 39(4).

Sun, X., Zhang, Y., Chen, G., & Gai, Z. (2017). Application of nanoparticles in enhanced oil recovery: a critical review of recent progress. Energies, 10(3), 345.

Tong, S., & Mohanty, K. K. (2016). Proppant transport study in fractures with intersections. Fuel, 181, 463-477.

Wang, S., Chen, C., Shiau, B., & Harwell, J. H. (2018). In-situ CO 2 generation for EOR by using urea as a gas generation agent. Fuel, 217, 499-507.

Yassin, M. R., Habibi, A., Eghbali, S., Zolfaghari, A., & Dehghanpour, H. (2017, October). An Experimental Study of Non-Equilibrium CO 2-Oil Interactions. In SPE Annual Technical Conference and Exhibition. Society of Petroleum Engineers.

Yu, M., Hussain, F., Arns, J. Y., Bedrikovetsky, P., Genolet, L., Behr, A., ... & Arns, C. H. (2018). Imaging analysis of fines migration during water flow with salinity alteration. Advances in Water Resources, 121, 150-161.

Yu, W., & Sepehrnoori, K. (2013, November). Simulation of proppant distribution effect on well performance in shale gas reservoirs. In SPE Unconventional Resources Conference Canada. Society of Petroleum Engineers.

Yuan, B., Ghanbarnezhad Moghanloo, R., & Pattamasingh, P. (2015, June). Applying method of characteristics to study utilization of nanoparticles to reduce fines migration in deepwater reservoirs. In SPE European Formation Damage Conference and Exhibition. Society of Petroleum Engineers.

Yuan, B., Moghanloo, R. G., & Zheng, D. (2016). Analytical evaluation of nanoparticle application to mitigate fines migration in porous media. Spe Journal, 21(06), 2-317.

Yuan, H., & Shapiro, A. A. (2010). Modeling non-Fickian transport and hyperexponential deposition for deep bed filtration. Chemical Engineering Journal, 162(3), 974-988.

Zheng, D. (2018). Pore-scale Modeling and Multi-scale Characterization of Liquid Transport in Shales.